Title

Optic Nerve Head Myelin-Related Protein, GFAP, and Iba1 Alterations in Non-Human Primates With Early to Moderate Experimental Glaucoma

Permalink

https://escholarship.org/uc/item/1rp0v8hn

Journal

Investigative Ophthalmology & Visual Science, 63(11)

ISSN

0146-0404

Authors

Chaudhary, Priya
Stowell, Cheri
Reynaud, Juan
et al.

Publication Date

2022-10-20

DOI

10.1167/iovs.63.11.9

Peer reviewed

Optic Nerve Head Myelin-Related Protein, GFAP, and Iba1 Alterations in Non-Human Primates With Early to Moderate Experimental Glaucoma

Priya Chaudhary,[1,2] Cheri Stowell,[1,2] Juan Reynaud,[1,2] Stuart K. Gardiner,[2] Hongli Yang,[1,2] Galen Williams,[1,2] Imee Williams,[1,2] Nicholas Marsh-Armstrong,[3] and Claude F. Burgoyne[1,2]

[1]Optic Nerve Head Research Laboratory, Devers Eye Institute, Legacy Research Institute, Portland, Oregon, United States
[2]Discoveries in Sight, Devers Eye Institute, Legacy Research Institute, Portland, Oregon, United States
[3]Department of Ophthalmology, University of California - Davis, California, United States

Correspondence: Claude F. Burgoyne, Optic Nerve Head Research Laboratory, Devers Eye Institute, Legacy Research Institute, 1225 NE 2nd Avenue, Portland, OR 97232, USA;
cfburgoyne@deverseye.org.

PURPOSE. The purpose of this study was to test if optic nerve head (ONH) myelin basic protein (MBP), 2′,3′-cyclic nucleotide 3′-phosphodiesterase (CNPase), glial fibrillary acidic protein (GFAP), and ionized calcium binding adaptor molecule 1 (Iba1) proteins are altered in non-human primate (NHP) early/moderate experimental glaucoma (EG).

METHODS. Following paraformaldehyde perfusion, control and EG eye ONH tissues from four NHPs were paraffin embedded and serially (5 µm) vertically sectioned. Anti-MBP, CNPase, GFAP, Iba1, and nuclear dye-stained sections were imaged using sub-saturating light intensities. Whole-section images were segmented creating anatomically consistent laminar (L) and retrolaminar (RL) regions/sub-regions. EG versus control eye intensity/pixel-cluster density data within L and two RL regions (RL1 [1-250 µm]/RL2 [251-500 µm] from L) were compared using random effects models within the statistical program "R."

RESULTS. EG eye retinal nerve fiber loss ranged from 0% to 20%. EG eyes' MBP and CNPase intensity were decreased within the RL1 (MBP = 31.4%, $P < 0.001$; CNPase =62.3%, $P < 0.001$) and RL2 (MBP = 19.6%, $P < 0.001$; CNPase = 56.1%, $P = 0.0004$) regions. EG eye GFAP intensity was decreased in the L (41.6%, $P < 0.001$) and RL regions (26.7% for RL1, and 28.4% for RL2, both $P < 0.001$). Iba1+ and NucBlue pixel-cluster density were increased in the laminar (28.2%, $P = 0.03$ and 16.6%, $P = 0.008$) and both RL regions (RL1 = 37.3%, $P = 0.01$ and 23.7%, $P = 0.0002$; RL2 = 53.7%, $P = 0.002$ and 33.2%, $P < 0.001$).

CONCLUSIONS. Retrolaminar myelin disruption occurs early in NHP EG and may be accompanied by laminar and retrolaminar decreases in astrocyte process labeling and increases in microglial/ macrophage density. The mechanistic and therapeutic implications of these findings warrant further study.

Keywords: immunohistochemistry, optic nerve head (ONH), lamina cribrosa, myelin, microglia, macrophages, monkey, experimental glaucoma (EG), astrocytes

The optic neuropathy of glaucoma includes pathophysiologic changes in the retina, optic nerve head (ONH), sclera, optic nerve, the mid-brain projections of the retinal ganglion cell (RGC) axons and the visual cortex.[1–4] Strong evidence suggests that a primary, multifactorial insult to the RGC axons within the lamina cribrosa of the ONH[5–11] leads to secondary alterations within the RGC soma, somal dendrites, and distal synapses that eventually lead to RGC death. However, the molecular mechanisms of glaucomatous axonal insult within the ONH remain poorly understood and there is critical need for therapies to complement intraocular pressure (IOP) lowering. Neuroprotective interventions that target the ONH tissues in glaucoma are few,[12–17] and currently far from clinical translation.

RGC axonal insult is central to vision loss in glaucoma and should therefore be central to its treatment. However, we have previously proposed that the defining pathophysiology of a glaucomatous optic neuropathy is deformation, remodeling, and physical disruption of the ONH load-bearing connective tissues (the perineural canal [pNC] sclera and lamina cribrosa) which contain the penetrating arterioles of the posterior ciliary arteries.[18–20] We view these connective tissue phenomena as interactive processes, driven by and driving astrocyte process remodeling,[21,22] phagocytosis of debris,[23] microglial and macrophage activation,[24,25] myeloid cell invasion,[26–29] fibroblast/myofibroblast transformation,[30,31] and oligodendrocyte loss.[32] We believe that these phenomena have primary and secondary effects on the adjacent RGC axons which contribute to RGC axonal injury and eventual RGC death.

In a series of papers, we suggested that laminar deformation,[33] remodeling,[34] and migration[35] in non-human

primate (NHP) early experimental glaucoma (EG) might also include recruitment of the immediate retrolaminar optic nerve fibrous longitudinal septa into the more transversely oriented (i.e. spanning the scleral canal and pial sheath openings), lamina cribrosa.[34] We hypothesized that these connective tissue processes might contribute to disruption of RGC axon homeostasis within the lamina cribrosa and RGC axon myelin homeostasis in the immediate retrolaminar optic nerve.[18–20]

Existing studies in mice and rats, provide evidence for active phagocytosis of myelin[36] and axonal mitochondria[21] within the myelin transition zone in genetic and experimentally induced glaucoma models. Myelin basic protein (MBP) and myelin oligodendrocyte glycoprotein (MOG) mRNA expression have been reported to be decreased in the optic nerve in a rat ischemia/reperfusion model.[37] Korneva et al.[38] demonstrated that the anterior extent of myelination moves posteriorly by measuring the distance from Bruch's membrane opening to the anterior boundary of MBP immunostaining in a mouse model of glaucoma. Whereas the ratio of the myelinated fiber area to the total optic nerve area was reported to be decreased in NHP EG,[39] this finding was reported in transverse orbital optic nerve sections 2 mm behind the scleral shell and was only present in the EG eyes of monkeys with severe axon loss. Although there are also reports of alterations in astrocytes and microglia/macrophages in mouse and rat models of glaucoma,[28,29,40–46] no attempt has been made to systematically study these phenomenon in NHPs with early EG.

The primary goal of this study was to introduce a novel, full-tissue-section, quantitative immunohistochemistry (qIHC) method that would allow anatomically consistent EG versus control eye detection of myelin-related protein (2′,3′-cyclic nucleotide 3′-phosphodiesterase (CNPase) and MBP) alterations within the immediate retrolaminar optic nerve in NHP early to moderate EG. A second goal of this study was to assess whether an astrocyte process marker (glial fibrillary acidic protein [GFAP]), a nuclei marker (NucBlue), and a surrogate marker of microglial/macrophage (ionized calcium binding adaptor molecule 1 [Iba1]) are altered within similar regions of the same NHPs with early EG eyes.

Our findings suggest that myelin related protein (CNPase and MBP) intensity and GFAP intensity are decreased within the EG eye laminar (GFAP only) and retrolaminar (CNPase,

MBP, and GFAP) regions of four NHPs with early to moderate unilateral EG. Our data also suggest that Iba1 positive (Iba+) and NucBlue pixel-cluster densities are increased within both the laminar and retrolaminar regions in the same EG versus control eyes.

METHODS

Animals

All animals were treated in accordance with the Association for Research and Vision in Ophthalmology (ARVO) statement for the use of animals in research and were approved by the Legacy Institutional Animal Care and Use Committee (IACUC; Protocols 07-09 and 10-07) which is authorized by the United States Department of Agriculture (USDA) license (92-R-0002) and is governed by an assurance with the Office of Laboratory Animal Welfare (A3234-01) as well as Legacy Policy (100.16). The Legacy Department of Comparative Medicine, which supervises all aspects of animal care, also maintains full Association for Assessment and Accreditation of Laboratory Animal Care (AAALAC) accreditation (Unit #000992). Four female NHP rhesus macaques (*Macaca mulatta*) were housed in a temperature and humidity-controlled room with a 12 hour light/12 hour dark cycle and provided with food and water ad libitum. Animal demographics are shown in Table 1.

Unilateral Experimental Glaucoma Model

Our NHP EG model has previously been described in detail.[47] Laser treatments were performed under ketamine only, ketamine and xylazine, or ketamine and dexmedetomidine anesthesia in two separate treatment sessions (180 degrees of the trabecular meshwork in each session, separated by 2 weeks). Laser treatments were repeated in subsequent weeks (but limited to a 90 degrees sector) until IOP elevation was detected or when post-laser IOP returned to normal levels before EG onset criteria were achieved in the lasered eye.

For this study, early EG was defined to be the onset of ONH surface change as revealed by longitudinal confocal scanning laser tomography (Heidelberg Retinal Tomography [HRT]; Heidelberg Engineering, Heidelberg, Germany) acquired during standard imaging sessions performed at

TABLE 1. Demographics, IOP Characteristics and Optical Coherence Tomography (OCT) Detected Experimental Glaucoma (EG) Eye Retinal Nerve Fiber Loss at the Time of Euthanasia

Animal #	Sex	Age, y	Weight, kg	Eye	Condition	Baseline Mean IOP, mm Hg[*]	Post-Laser Mean IOP, mm Hg	Post-Laser Peak IOP, mm Hg	EG Eye Cumulative IOP Insult, mm Hg x Day[†]	IOP at the Time of Euthanasia, mm Hg[‡]	EG Eye Percent RNFLT Loss at Euthanasia[§]
NHP 1	F	15	7.2	OS	C	11.7	10.7	14.0	470.5	10.6	
				OD	EG	12.8	15.7	41.3		23.3	4/0
NHP 2	F	13	4.5	OS	C	12.3	11.2	15.0	868.7	8.6	
				OD	EG	13.0	29.0	50.7		13.3	−18.1/−15.6
NHP 3	F	11	5	OS	C	11.8	11.2	16.7	549.5	9.6	
				OD	EG	12.8	19.5	38.3		26.6	−8.9/−10.7
NHP 4	F	6	6.7	OS	C	10.9	10.3	13.3	663.7	9.0	
				OD	EG	11.4	13.9	30.7		26.3	−5.9/1

[*] Baseline mean IOP C/EG (mm Hg) – "C" for control eyes; "EG" for experimental glaucoma eyes.
[†] Cumulative IOP insult – the difference between the EG versus C eye area under the post-laser IOP curves expressed in mm Hg × days.
[‡] IOP at the time of euthanasia – the IOP recorded when the animal arrived in the necropsy room.
[§] EG eye percent RNFLT loss at euthanasia - data are EG/C at the time of euthanasia (left) and EG at the time of euthanasia/EG at baseline (right).
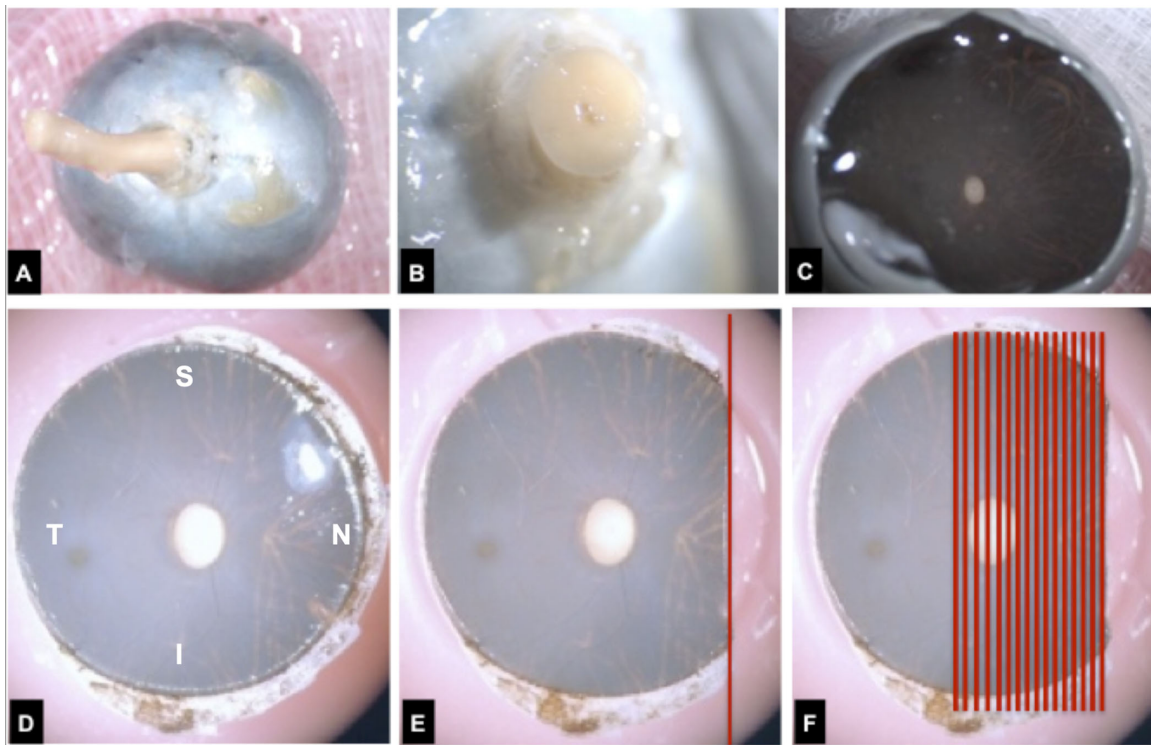
FIGURE 1. **Optic nerve head (ONH) tissue processing for IHC.** See the Methods section for our definition of the ONH and neural canal. (**A**) Following euthanasia by exsanguination during perfusion fixation with 4% paraformaldehyde, each globe was enucleated and all peri-ocular connective, muscle, and fat tissues were removed. (**B**) The orbital optic nerve (ON) was cut away from the globe leaving a 2 to 3 mm ON stump. (**C**) The globe was opened, the vitreous removed, and (**D**) a 10 mm trephine (circular cutting blade) was used to remove the ONH and adjacent posterior pole tissues including the fovea (S – superior; I – inferior; N – nasal; T – temporal). (**E**) A vertical cut (see methods) was made on one side of the ONH trephine, the tissues were paraffin embedded with the vertical cut at the block face, producing serial, vertical, 5 µm sagittal sections (red lines). (**F**) The clinical location of each section was then estimated on a fundus photograph using common anatomic landmarks (see Fig. 2).

baseline (3-5 individual sessions prior to laser) and every 1 to 2 weeks post-laser (i.e. following the onset of unilateral laser to the trabecular meshwork to induce experimental IOP elevation).[48] Our definition of HRT-detected ONH surface change required confirmation from two subsequent imaging sessions. Longitudinal optical coherence tomography (OCT) measurements of retinal nerve fiber layer (RNFL) thickness (standard 3.5 mm circle scan) were also performed, but not used in defining EG onset.

IOP was measured at the start of each imaging or laser session by Tonopen XL (Reichert Inc., Depew, NY, USA) in both eyes of each animal (mean of $n = 3$ measures per eye) following an induction dose of ketamine (15 mg/kg IM) and either xylazine (0.8–1.5 mg/kg IM) or midazolam (0.2 mg/kg IM).

Euthanasia and Post-Mortem Tissue Processing

All animals were euthanized by pressurized (25 to 35 mm Hg) 4% paraformaldehyde perfusion fixation (made fresh a day before perfusion, kept at 4°C) delivered via a catheter into the left ventricle of the heart under deep isoflurane anesthesia. Eyes were enucleated after perfusion fixation. For each eye, (Fig. 1A) orbital tissues were removed, the orbital ON was cut 3 mm behind the globe (Fig. 1B), and the globe was opened 3 mm posterior to the scleral-corneal limbus (Fig. 1C). Eyes were further immersed in 4% paraformaldehyde for 24 hours. The ONH tissues were

trephined (10 mm) using a circular blade (Fig. 1D). The position of the fovea relative to the optic disc was used to define the naso-temporal axis and used as a guide during embedding and sectioning (Fig. 1E). The 10-mm circular piece of ONH tissue was centered on the optic disc and isolated using a circular trephine blade and trimmed to create a vertical edge for cutting (Fig. 1E). The trephined ONH tissue was then embedded in paraffin with the vertical cut edge facing down (i.e. on the block face), and serial 5 µm sections were cut through the ONH and macula (Fig. 1F). Two sections were captured and mounted on each individual Superfrost plus glass slide (EMS, Cat # 71869-10) and stored at room temperature.

Estimating the Clinical Location of Each Vertical ONH IHC Paraffin Section

To choose best-matched EG and control eye sections from similar ONH regions within the EG and control eyes of each animal, as well as picking equivalent regions between the EG and control eyes of all animals, the location of each EG and control eye paraffin section was first estimated using an ONH color photograph of the sectioned eye, as follows. For each eye, nasal and temporal "cardinal" sections that marked the transition from an "intact" to an "open" Bruch's membrane (i.e. containing two Bruch's membrane opening [BMO] points) were determined. Either those sections, or adjacent sections that provided a larger distance between the two BMO points, were dewaxed and stained using standard
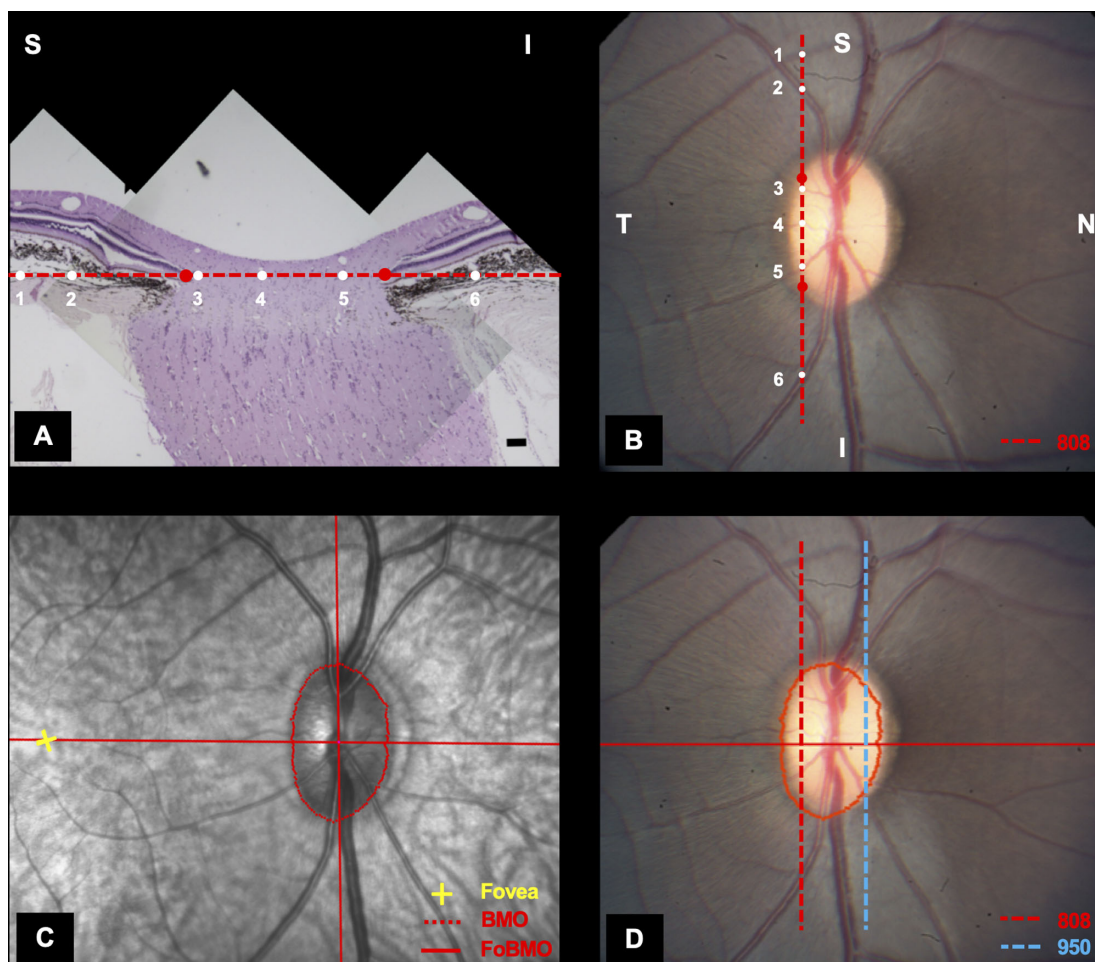
FIGURE 2. Estimating the clinical location of temporal and nasal "cardinal" ONH paraffin sections relative to the OCT foveal-BMO (FoBMO) axis. See the Methods section for our definition of the ONH and neural canal. (**A**) The temporal cardinal section (number 808 - *red dotted line* in panels **A**, **B**, and **D**) from the left (control) eye (shown in the right eye orientation) of NHP 3 was stained using hematoxylin and eosin (H&E) and the location of each blood vessel (6 *white circles* numbered 1 to 6 also in *white*) and BMO point (*red circles*) was identified and projected to the BMO reference line (*red dotted line* in panels **A**, **B**, and **D**). (**B**) The superior (S) versus inferior (I) orientation and temporal versus nasal location of the section (*red dotted line*) is estimated by adjusting the angle of the section line until the best fit of the BMO and vessel points (1 to 6 in *white* from panel **A**) to the photograph is accomplished. Estimating the location of a nasal cardinal section (section 950 – *blue dotted line* in panel **D**) was then performed in a similar manner. (**C**) The OCT-determined foveal to BMO centroid (FoBMO) axis as projected onto the infrared (IR) image acquired at the time of OCT image acquisition during the pre-euthanasia imaging session. (**D**) The location and orientation of the temporal (808) and nasal (950) cardinal tissue sections relative to the OCT-determined FoBMO axis is achieved by colocalizing the color fundus image containing their locations to the OCT IR image using the retinal vessels. The nasal/temporal position and S versus I orientation of each individual IHC section is then approximated relative to the cardinal sections by using the section number and fine-tuned using the vessel crossings and BMO points as outlined above.

hematoxylin and eosin (H&E) then imaged at 5× magnification (Fig. 2A). Within each section image, the two BMO points as well as the center of each identifiable vessel were identified. Using a line connecting the two BMO points as a reference, the location of the center of each vessel was projected to this BMO reference line. This line, along with its vessel projection points, was then overlaid on a fundus image and affine-transformed,[49] until the position of best fit for both the BMO points (to the clinical disc margin) and central vessel points (to retinal and optic disc vessels) was obtained (Fig. 2B). The location of both cardinal sections relative to the OCT determined foveal to BMO (FoBMO) centroid axis (Fig. 2C) was obtained by colocalizing the ONH fundus photograph containing the location of the two cardinal section images to the OCT infrared (IR) image acquired at the time of OCT data acquisition (Fig. 2D).[47] The nasal/temporal position and superior/inferior orienta-

tion of each individual IHC section was then approximated relative to the cardinal sections by using the section number and fine-tuned using the vessel crossings and BMO points, as outlined above.

Histologic ONH and Neural Canal Definitions

We define the ONH (see Figs. 1, 2) to include the tissues within the neural canal and those immediately adjacent to it, namely, the peri-neural canal (pNC) retina, choroid, and sclera as well as the immediate retrolaminar (RL) optic nerve (Fig. 3).[18,50,51] We define the neural canal to be the connective tissue pathway extending from the BMO (see Fig. 2) through the choroid and sclera through which the RNFL axon bundles achieve the retrolaminar optic nerve.[52–54] Within the ONH, this study reports qIHC findings within the laminar and retrolaminar regions only, compar-
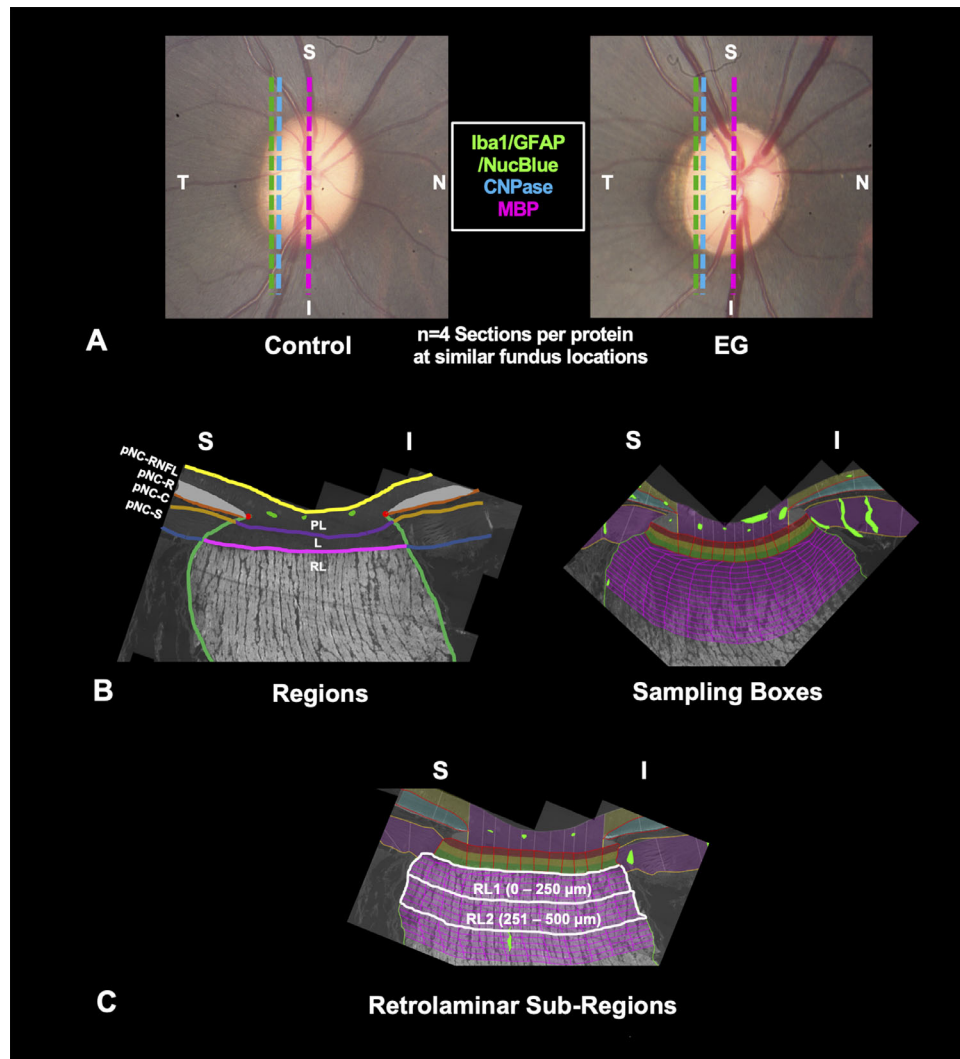
FIGURE 3. Quantitative immunohistochemical (qIHC) comparisons within anatomically consistent laminar and retrolaminar ONH regions, subregions, and sampling boxes of EG versus control eyes. Representative images from NHP 2 are used to illustrate clinical and anatomic relationships. (**A**) Best-matched EG and control eye clinical location of four IHC sections for each protein relative to the OCT-determined Foveal-BMO (FoBMO) axis (*red line*) and segmented Bruch's Membrane Opening (BMO; *red points*; see Fig. 2, and the Methods section). (**B**) Using the segmented anatomic landmarks from the polarized light image of each IHC section, each IHC section fluorescence image was divided into laminar (L) and retrolaminar (RL) optic nerve (ON) regions for this study. Additional prelaminar and perineural canal (pNC) RNFL, choroid, and sclera regions were also segmented but are not included in this study and will be the subject of future reports. The laminar and RL regions were then automatically subdivided into proportionally consistent superior (S) to inferior (I) sampling boxes (*right*, see the Methods section) using custom software. (**C**) Retrolaminar RL1 (0–250 µm) and RL2 (251–500 µm) subregions. Only the first 10 retrolaminar bands were analyzed due to short retrolaminar nerves in some animals. In some animals, only the RL1 region was present (see Table 2 for NHP RL1 and 2 availability). Note that whereas the inner (*red*), middle (*yellow*), and outer (*green*) laminar subregions are automatically generated and depicted in the maps, laminar subregions were pooled and statistical analyses have been performed and reported as "laminar" data for this report. Our ability to closely match the EG and Control eye FoBMO location of the IHC sections among and between animals was limited for some NHPs and/or some IHC targets (see the Methods and Discussion sections).

ing EG versus control eye protein alterations within (animal specific) and among (experiment wide) four NHPs with unilateral EG.

IHC in EG and Control ONH

IHC was performed within three individual runs on four best matched EG and control eye tissue sections per animal. For each qIHC run, two glass slides containing four adjacent or near-adjacent paraffin sections were chosen from similar optic nerve head regions from both the EG and control eyes of each animal (Fig. 3A). However, for some IHC runs, close matches for the clinical location of the EG and control eye sections for individual animals could not be achieved due to the loss of sections in one eye, differences in the cutting angle between the control and EG eyes, or, in a single instance, due to inadvertent error (see Results and Discussion sections) (Fig. 4). For each IHC run, the four paraffin sections from both eyes of 4 NHPs ($n = 32$ sections total) were processed together through the following steps during a 2-day processing period: dewaxed in xylene, dehydrated in ethanol solutions (100%, 95%, 70%, and 50%); rehydrated with water, and then washed in phosphate buffered saline (PBS) for 10 minutes.

The sections were then incubated with 0.1% Triton X-100 and blocked with bovine serum albumin and serum
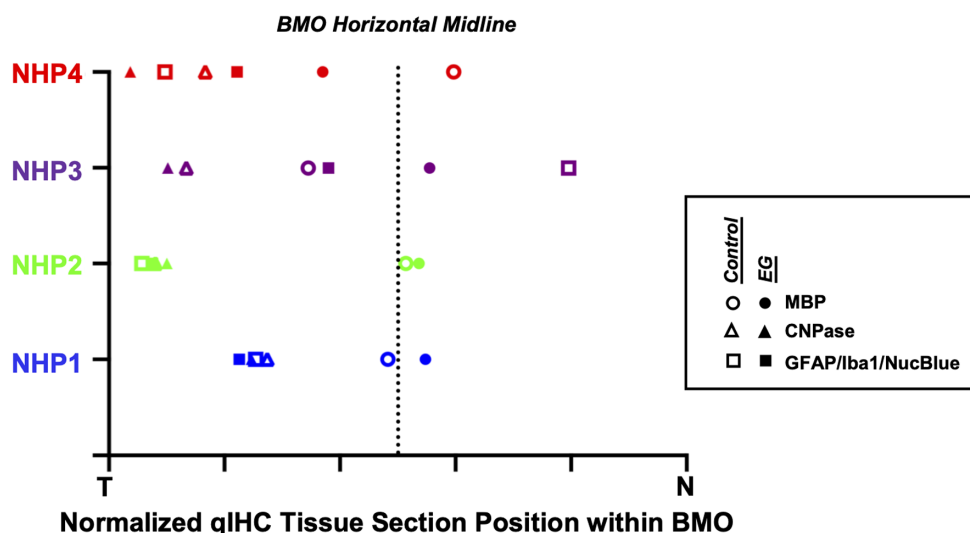
FIGURE 4. Normalized location of the four vertical IHC sections for each study eye and each qIHC target protein relative to the nasal and temporal extents of Bruch's membrane opening (BMO). Data are plotted in right eye orientation. Data point symbols are colored for each NHP and are open for control eyes and filled for experimental glaucoma (EG) eyes (see legend above for Fig. 3). The x-axis position of each data point represents an estimate of where the vertical sections crossed the FoBMO axis and are normalized relative to the horizontal midline and the nasal and temporal BMO points. The superior and inferior orientation of each section is separately confirmed using the central retinal vessels, as explained in the Methods section and Figure 2. By looking up and down and comparing the relative location of each open or closed symbol it is apparent that for most qIHC targets the transverse clinical location of the sections for each study eye are acceptably close. However, for NHP 3, it was retrospectively noted (after IHC had been completed) that the position of the EG eye sections for the GFAP, Iba1, and NucBlue were inadvertently selected from the mid-nasal rather than the mid-temporal ONH. While the proper superior versus inferior orientation of these sections was confirmed, the EG versus control eye section locations were least well matched for these targets (see the Discussion section).

(same species as the secondary antibody). Run 1 sections were incubated with MBP (myelin = 1:40, AbD Serotec catalog 0300-0082, rabbit). Run 2 sections were incubated with CNPase (myelin = 1:50, Cell Signaling Technology catalog 5664, rabbit). Run 3 sections were incubated with Iba1 (microglia/macrophages = 1:50, Thermo Fisher, PA5-27436, rabbit, verified by Thermo Fisher on knockouts to ensure that the antibody is specific), and GFAP (astrocytes = 1:400, Thermo Fisher, PA1-10004, chicken, advanced verified by Thermo Fisher by relative expression studies) primary antibodies overnight at 4°C in a humidified chamber. For each run, the sections were washed with PBS 3 times (5 minutes each wash), and incubated with Cy3 conjugated donkey anti rabbit (Jackson Immuno Research Laboratories, 711-165-152, 1:500 in PBS) for 1 hour at room temperature or goat anti chicken or rabbit Alexa Fluor 488/568/647 (1:200, Thermo Fisher, A11039, A11011, or A21245) in PBS for 2 hours at room temperature. Run 3 had NucBlue (nuclei) in blue, GFAP in green, and Iba1 in far red. These filters (blue = Leica 513824, Ex BP360/40 Em BP460/50 dichroic 400, green = Chroma C160017 FITC, HQ480/40x [EX] HQ535/50 m [EM] Q505Ip [BS], far red = Chroma C163860, ET640/30x [EX] T660lpxr [BS] ET690/50 m [EM]) had sufficient bandwidth separation, thus avoiding any bleed through.

For negative control sections ($n = 2$ sections from the control and EG eye of one animal for each run), the secondary antibodies were applied but the primary antibodies were withheld. An additional no-primary-antibody and no-secondary-antibody control was used to detect any background fluorescence. The run 3 sections (stained with GFAP and Iba1) were mounted in antifade containing NucBlue nuclear dye (Thermo Fisher, P36981) for cell density assessment.

Image Acquisition

After staining, each section was imaged on an inverted microscope (DM IRB, Leica Microsystems GmbH) using a 40× apochromatic objective, 0.75 NA (Leica Microsystems GmbH) at the appropriate wavelengths red (Chroma 49004 cube), green (Chroma C160017 cube), far-red (Chroma C163860 cube), and blue (Leica 513824 cube) using an LED light source (Lumen Dynamics X-Cite 120), a 2758 × 2208 pixel grayscale camera (Retiga 6000, Q Imaging, Surrey, British Columbia, Canada), and a computer-controlled X-Y-Z stage (Applied Scientific Instrumentation, Inc., Eugene, OR, USA). The filter cubes were chosen so that there is no bleed-through between channels. Images were acquired in a dark room. Individual tiles (8 bit) were acquired with a 10% overlap to cover the entire area of interest. After fluorescent imaging was completed, each section was imaged using a 10× objective with a polarized lens. These polarized images were used to delineate the ONH, RL, L, sclera, neural boundary, retina, and choroid (see Fig. 3) because they provided better contrast and made it easier to identify these features. Custom software was developed to control the X-Y-Z stage, microscope, camera, focus, and illumination during the primary image acquisition. Image composites for both fluorescent and polarized images were assembled using custom software.

Focusing at each location was performed by sweeping the stage from the lowest to highest defined Z in 0.5 micron increments and capturing an image at every step. The maximum pixel variance from three regions in every image of the stack was then calculated and stored in an array. This pixel variance increased as the focal plane was reached, indicating sharper focus and larger contrast. To eliminate noise in the variance array, a Gaussian curve was fitted to the vari-

ance profile. The Z at the peak was then selected as the focal plane at that location.

Once image acquisition for each IHC section was completed, blue-channel images underwent an illumination correction step as each 40× blue-channel image was noted to be consistently uneven (i.e. the center of each 40× image being brighter than the periphery). To correct this, a reference 40× blue channel illumination image was acquired using a calibration slide. The image was then smoothed with a 25 × 25-pixel Gaussian filter to isolate the low frequency components of the illumination pattern intrinsic to the imaging system. Finally, the 40× reference image was normalized to the brightest pixel. All 40× blue-channel images were then illumination-corrected by dividing every pixel by its corresponding pixel in the 40× reference image.

Manual Segmentation of ONH Anatomic Landmarks Within the Composite Images of Each Paraffin Section

Using custom software (ATL 3D Suite, Fortune et al.[55]), the following ONH landmarks were segmented within the polarized composite image for each section: internal limiting membrane (ILM), BMO, Bruch's membrane, outer RNFL boundary, anterior and posterior scleral surface, anterior and posterior laminar surface, neural canal boundary, posterior choroidal surface (if the retina and choroid are lifted away

from the sclera within a section), and all large blood vessels or tears in the tissue (see Fig. 3B).[56–60]

Anatomically Consistent Laminar and Retrolaminar Optic Nerve Regions, Subregions, and Sampling Boxes for EG Versus Control Eye Comparisons

Using the segmented anatomic landmarks outlined above, each qIHC tissue section was divided into laminar and retrolaminar optic nerve regions: RL1 (0–250 μm) and RL2 (251–500 μm). Additional prelaminar and pNC-RNFL, pNC-choroid, and pNC-sclera regions were also segmented but are not included in this study and will be the subject of future reports. Each laminar and retrolaminar tissue region was subdivided into a proportionally consistent set of sampling boxes that could be consistently applied to all experimental and control eye section images (see Figs. 3B, 3C).

Sample Box Signal Intensity, NucBlue, and Iba1+ Pixel Cluster

Large vessels and regions of tissue disruption within each section were manually delineated and masked so as to exclude them from sample box signal calculations (see Fig. 3B). For each sampling box of a paraffin section, the signal intensity density (hereafter referred to as "signal intensity"
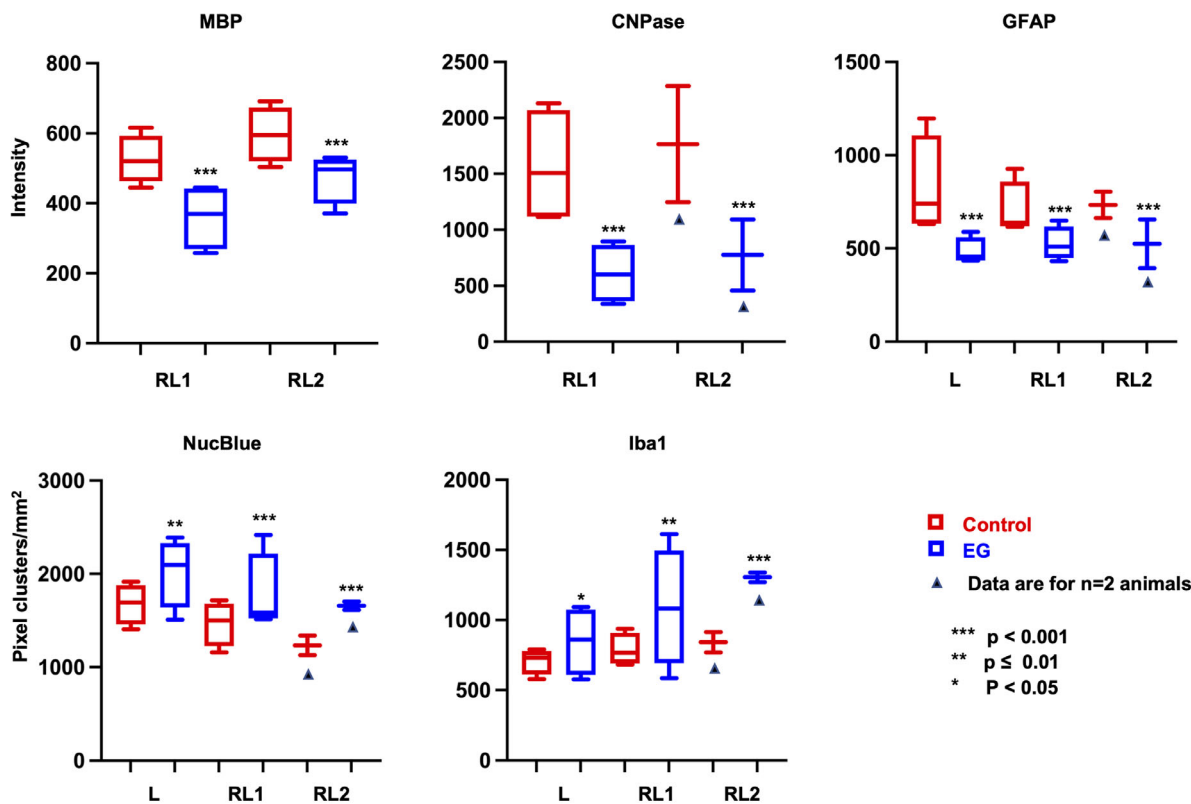

FIGURE 5. **Graphic display of experiment-wide qIHC by target and region**. CNPase, MBP, and GFAP fluorescence intensity per unit area as well as NucBlue and Iba1 pixel-cluster per mm² are displayed. Values in the boxes are 25th to 75th percentile and whiskers are plotted minimum to maximum. Significance is shown by asterisks (also see Table 2). In NHPs 1 and 4, the retrolaminar nerve within the paraffin sections was short and the RL2 region therefore could not be analyzed for all antibodies except MBP (shown by underlying *black triangle*). Experiment-wide data for the RL2 region for CNPase, GFAP, NucBlue pixel-cluster density, and Iba1 cluster density is thus based on two animals (NHPs 2 and 3). See Supplementary Table S1 for actual data.
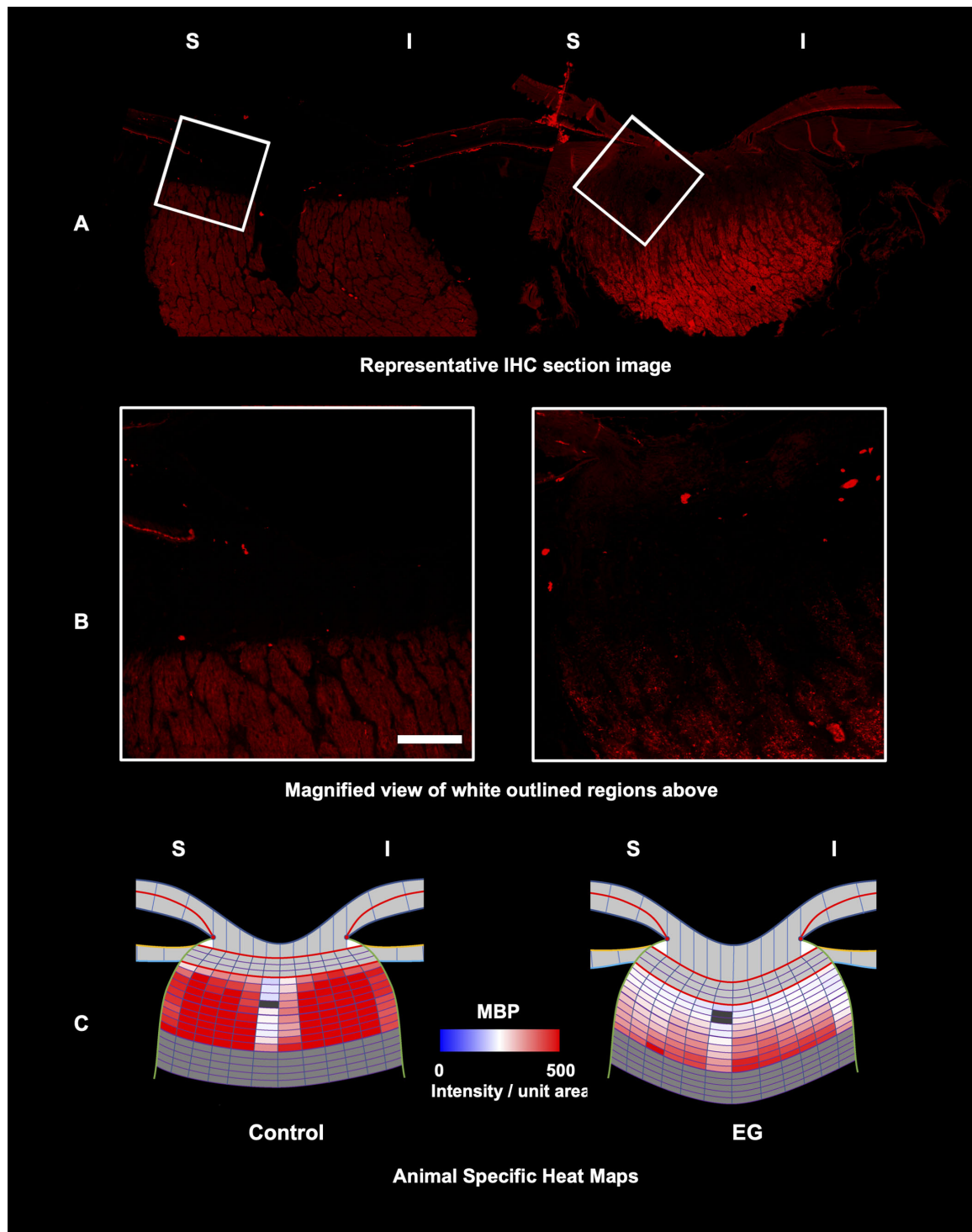
FIGURE 6. MBP intensity decreased in the EG eye retrolaminar regions. Representative control (*left*) and EG (*right*) eye single IHC section images (**A**, **B**) and animal-specific mean intensity heat maps (**C**) for MBP for NHP2. **A** Control and EG eye fluorescent full section images (see Fig. 3A for the clinical location of these sections), with magnified views of the white outlined regions shown in **B**. (**C**) MBP intensity heat maps for NHP2 based on mean data for four section images from each eye reveal diffuse qualitative decreases in both retrolaminar RL1 and RL2 subregions (see Fig. 3), which achieve significance by statistical analysis (see Table 2, Supplementary Table S1). *Dark grey* color denotes blood vessels.

was computed by integrating the intensity [grayscale value] of all pixels within its boundary and dividing the sum by the box's area; i.e. intensity per unit area). Only valid pixels were included in this calculation; thus, if a pixel fell within the boundaries of a vessel or other invalid regions, it was excluded. The signal intensity and the area of each sampling box were reported and stored as comma separated values (.csv) for subsequent analysis (see Fig. 5). This analysis was
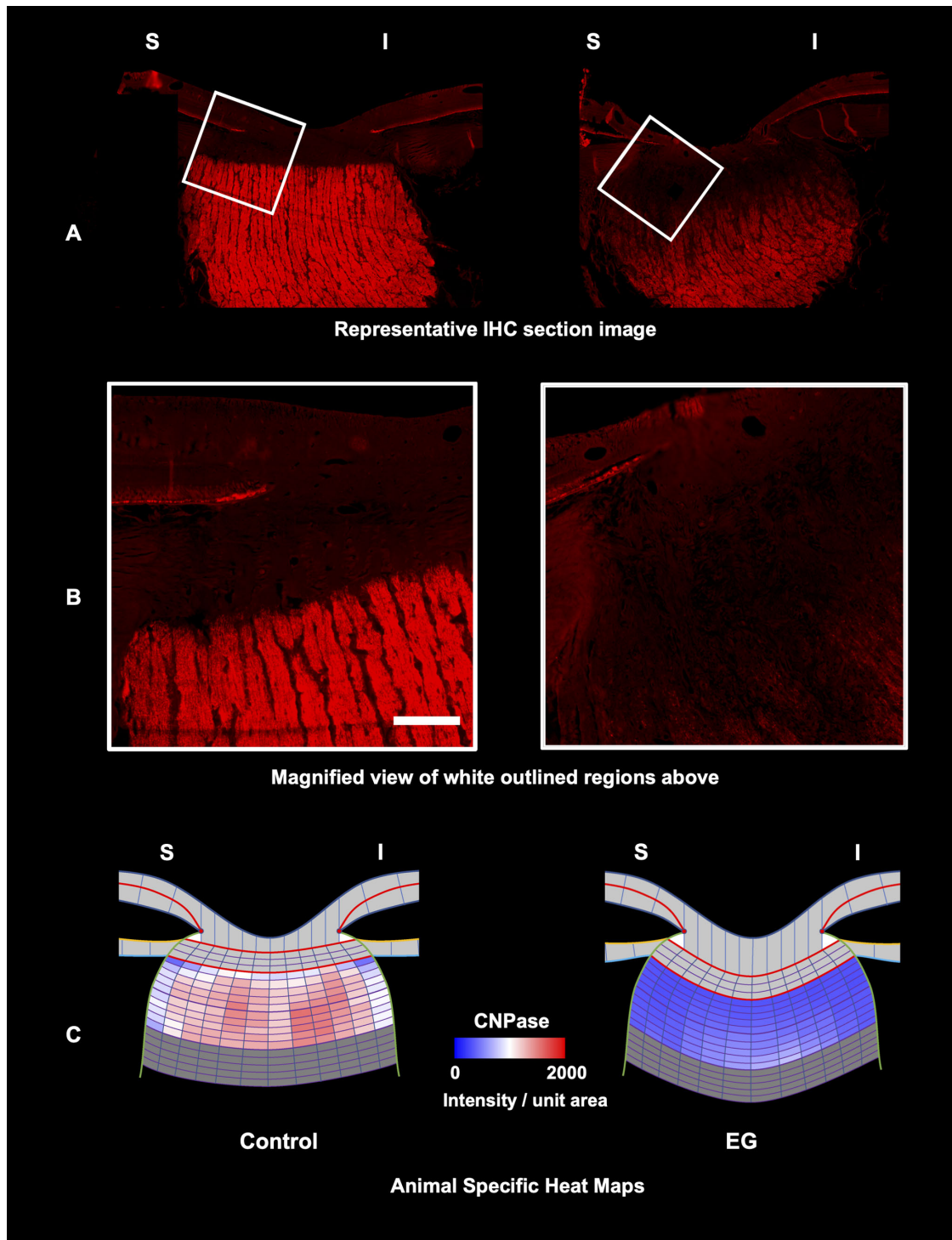
FIGURE 7. CNPase protein intensity decreased in the EG eye retrolaminar regions. Representative control (*left*) and EG (*right*) eye single IHC section images (**A**, **B**) and animal-specific mean intensity heat maps (**C**) for CNPase for NHP2. **A** Control and EG eye fluorescent full section images (see Fig. 3A for the clinical location of these sections), with magnified views of the white outlined regions shown in **B**. **C** CNPase intensity heat maps for NHP2 based on mean data for four section images from each eye reveal diffuse qualitative decreases in both retrolaminar RL1 and RL2 subregions (see Fig. 3), which achieve significance by statistical analysis (see Table 2, Supplementary Table S1).

done for MBP (Fig. 6), CNPase (Fig. 7), and GFAP (Fig. 8) only.

For MBP, CNPase, and GFAP signal intensity data, laminar (GFAP only), and retrolaminar data are reported without negative control or background subtraction because both

the negative control and background levels were modest, similar for both EG and control eyes, and their subtraction did not affect the significance of EG versus control eye differences. However, whereas the detected MBP and CNPase fluorescence within the laminar region was not considered
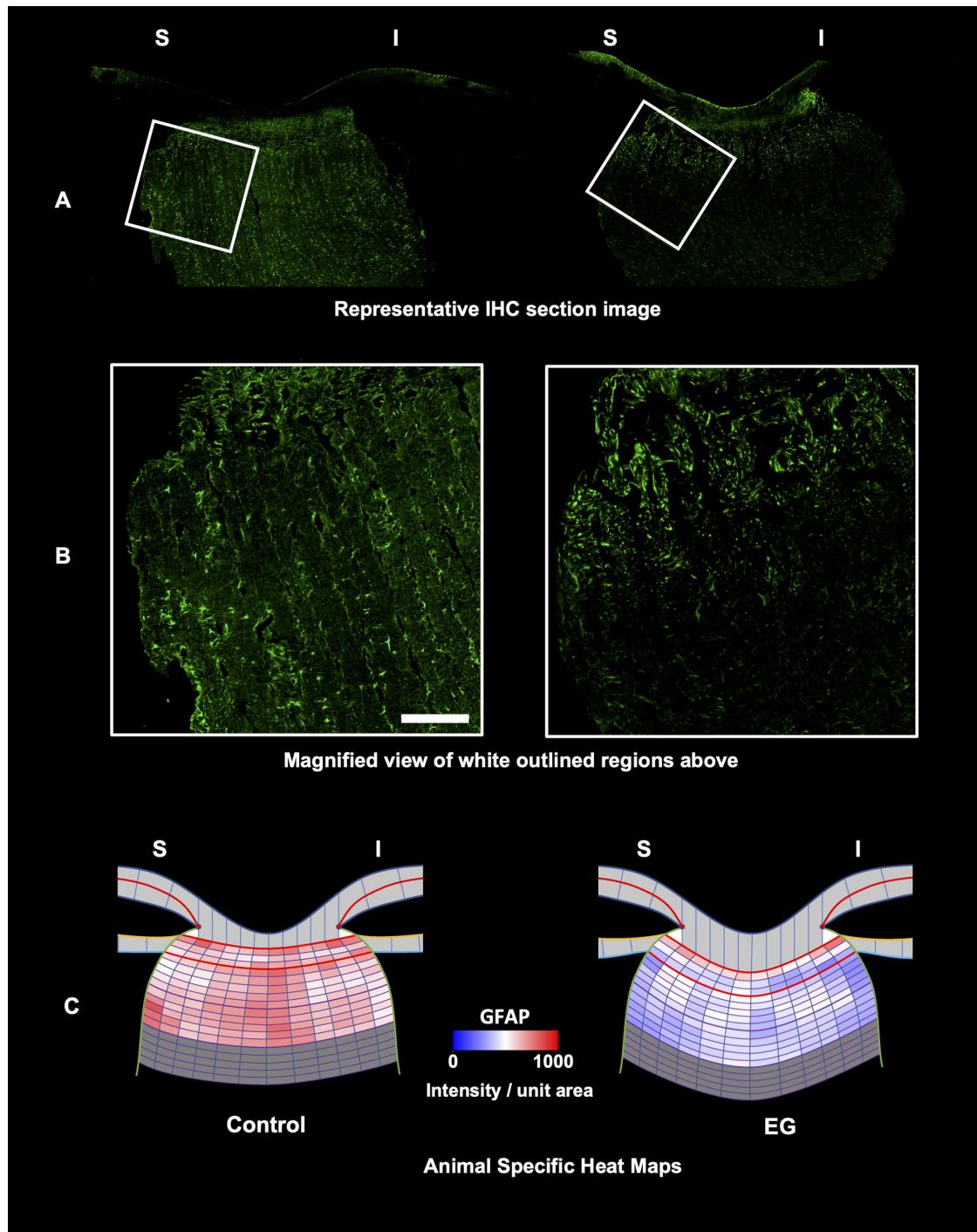
FIGURE 8. GFAP intensity decreased in the EG eye laminar and retrolaminar regions. Representative control (*left*) and EG (*right*) eye single IHC section images (**A**, **B**) and animal-specific mean intensity heat maps (**C**) for GFAP for NHP2. **A** Control and EG eye fluorescent full section images (see Fig. 3A for the clinical location of these sections), with magnified views of the white outlined regions shown in **B**. **C** GFAP intensity heat maps for NHP2 based on mean data for four section images from each eye reveal diffuse qualitative decreases within the laminar and both retrolaminar (RL1 and RL2) subregions (see Fig. 3), which achieve significance by statistical analysis within the retrolaminar regions (see Table 2, Supplementary Table S1).

signal (and was therefore reported as "not present" ["NP"] - see the Results section), the detected intensity for both antibodies within the lamina was consistently higher in the control versus the EG eyes. Although we report unsubtracted RL data for both antibodies, we performed a separate anal-

ysis of the RL data for both MBP and CNPase in which, for each NHP, the mean intensity of the laminar sampling boxes for the four control eye sections were subtracted from each RL sampling box of each control eye section and the same was separately done for the EG eye RL data. Using the
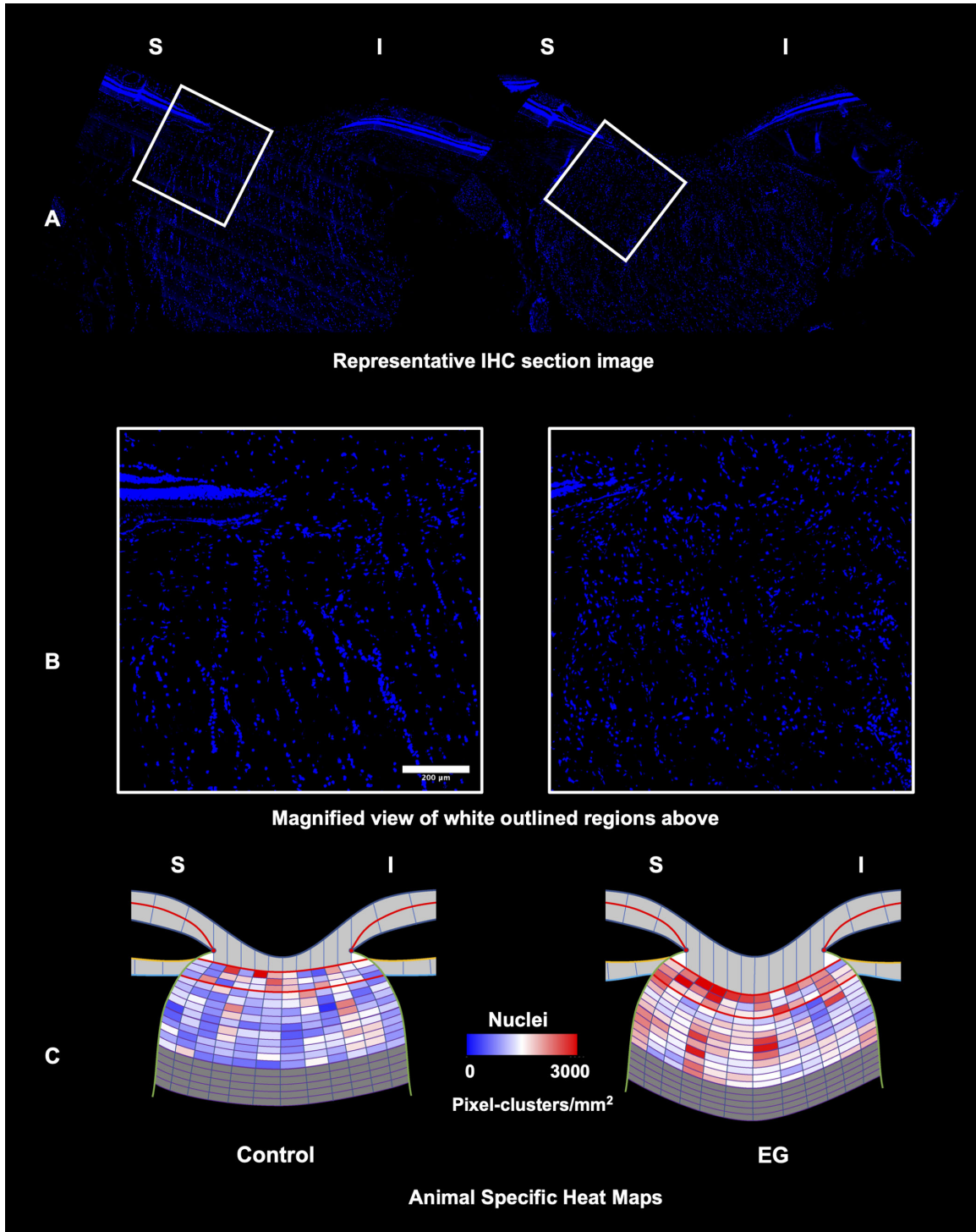
FIGURE 9. **NucBlue pixel-cluster density increased in the EG eye laminar and retrolaminar regions**. Representative control (*left*) and EG (*right*) eye single IHC section images (**A**, **B**) and animal-specific mean intensity heat maps (**C**) for NucBlue pixel cluster density for NHP2. **A** Control and EG eye fluorescent full section images (see Fig. 3A for the clinical location of these sections), with magnified views of the white outlined regions shown in **B**. **C** NucBlue pixel cluster density heat maps (see the Methods section) for NHP 2 based on mean data for four section images from each eye reveal diffuse qualitative in the laminar and both retrolaminar RL1 and RL2 subregions (see Fig. 3), which achieve significance by statistical analysis for both retrolaminar regions (see Table 2, Supplementary Table S1).

"lamina-subtracted" control and EG eye RL data for all four NHPs, a second statistical analysis was performed and all significant RL findings (as reported in the Results section), remained significant.

For NucBlue (Fig. 9) and Iba1+ pixel-cluster density (Fig. 10) computations, a threshold was first applied to each sampling box (corresponding to the mean intensity + 2 standard deviations of the region in which the sampling box was
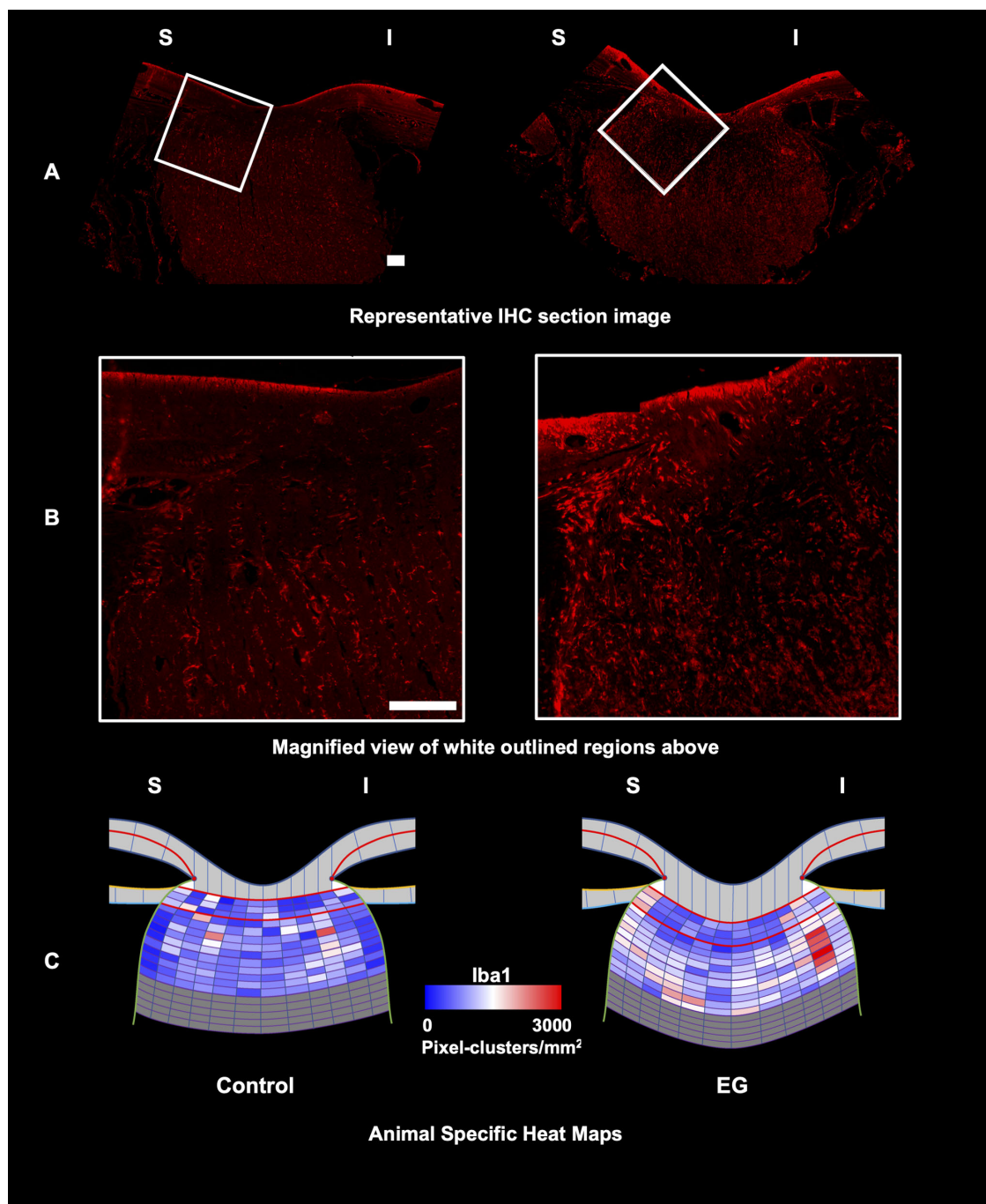
FIGURE 10. **Iba1+ pixel-cluster density increased in the EG eye laminar and retrolaminar regions**. Representative control (*left*) and EG (*right*) eye single IHC section images (**A**, **B**) and animal-specific mean intensity heat maps (**C**) for Iba+ pixel-cluster density for NHP 2. A Control and EG eye fluorescent full section images (see Fig. 3A for the clinical location of these sections), with magnified views of the white outlined regions shown in **B**. **C** MBP intensity heat maps for NHP2 based on mean data for four section images from each eye reveal diffuse qualitative decreases in both retrolaminar RL1 and RL2 subregions (see Fig. 3) which achieve significance by statistical analysis (see Table 2, Supplementary Table S1).

located). To remove any remaining noise, a 3 × 3 median filter was applied. In the resulting binary image, holes were filled and a watershed algorithm was applied to separate NucBlue or Iba1+ pixel clusters.[61] NucBlue or Iba1+ pixel clusters were then counted using the ImageJ Particle Analyzer,[62] keeping particles that were equal to or larger than 50 pixels regardless of shape. Identified NucBlue or Iba1+ pixel clusters that touched the edges of any sampling box were not included in the count.

Animal-Specific and Experiment-Wide qIHC Statistical Analyses

All laminar and retrolaminar intensity and pixel-cluster density analyses were plotted as heatmaps (Fig. 11) for qualitative interpretation and hypothesis generation. Statistical analyses were performed using the R software, version 4.0.3 (2020-10-10; The R Foundation for Statistical Computing, Vienna, Austria, downloadable from http://www.R-project.
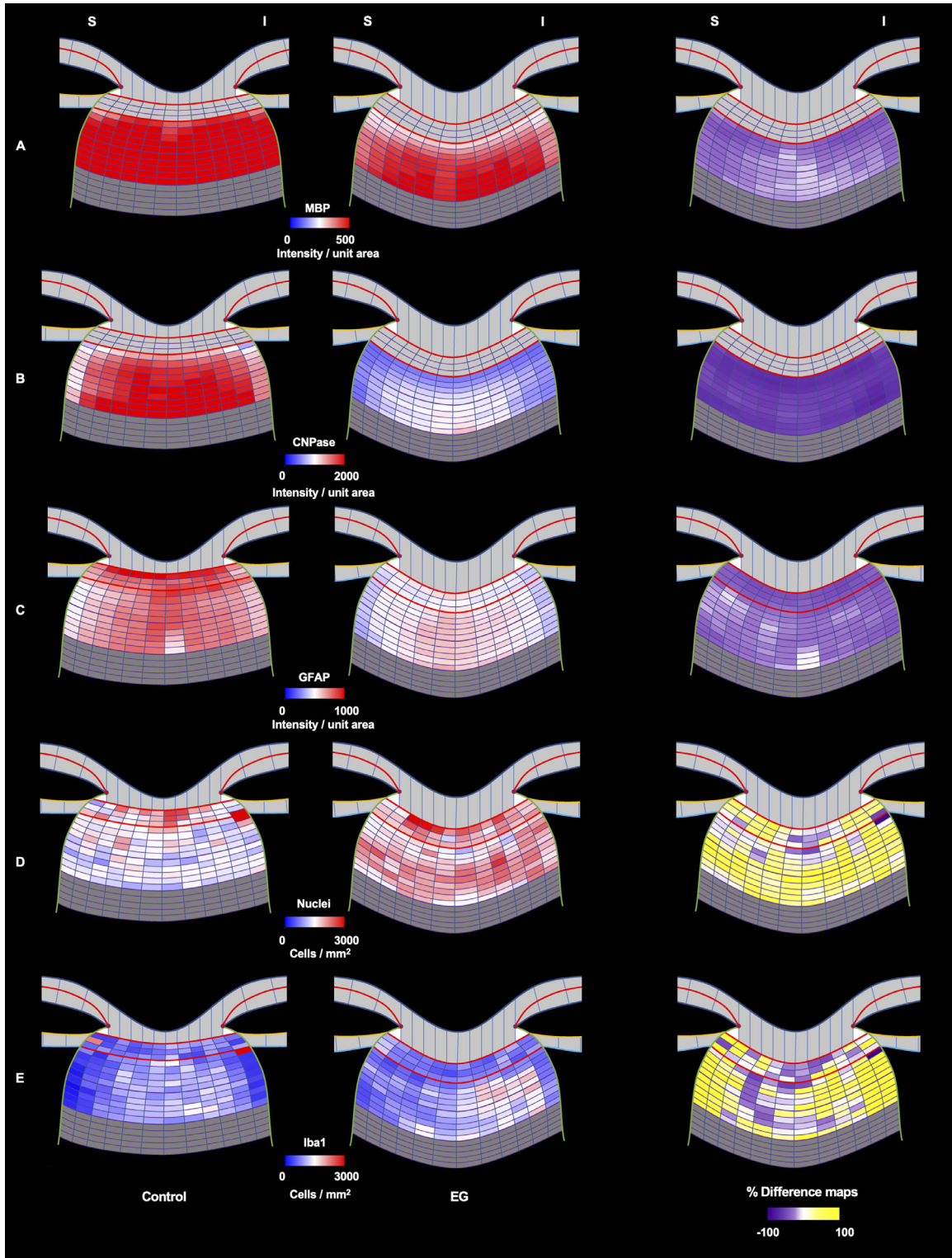
FIGURE 11. Experiment wide ($n = 4$ NHPs and $n = 16$ sections) control (*left*) versus EG (*middle*) eye heatmaps and percent difference maps (*right*) for all protein, pixel cluster, and cellular density targets. EG versus control eye differences in the inferior compared to superior subregions were not significantly different for any target. Percent difference maps were calculated using the formula (EG-C)*100/C.

org/). For MBP, CNPase, and GFAP, the average signal intensity for each tissue region or subregion was compared between the EG and control eyes using a series of linear mixed effects models; and the NucBlue and Iba1+ pixel-

cluster densities within the same regions were compared using Poisson mixed effects models. For each fluorescent signal, EG versus control eye differences were assessed experiment-wide (for all 4 animals overall) within a random

effect for each section nested within random effects for each animal. A continuous autoregressive correlation structure was used to account for adjacency of sampling boxes. EG versus control eye differences were also assessed within each animal individually, omitting the animal-level random effect.[63]

RESULTS

Longitudinal OCT Confocal Scanning Laser Tomography (CSLT) and Retinal Nerve Fiber Layer Thickness (RNFLT) Data Suggests That the Stage of EG We Studied Ranged From Early (NHP 1, 3, and 4) to Moderate (NHP 2) EG.

Animal demographics, IOP data, and EG eye OCT RNFL thickness thinning at the time of euthanasia are reported for each animal in Table 1. EG eye RNFL thinning compared to baseline ranged from 0% in NHP 1 and NHP 4, to 10.7% in NHP 3 and 15.6% in NHP 2. While orbital optic nerve axon counts were not performed in these animals, this range of RNFL thinning corresponds to approximately 0 to 30% optic nerve axon loss in NHP 1, 3, and 4 and 20% to 40% axon loss in NHP2.[64,65] In a previous study[53] of 8 early EG animals euthanized using the same CSLT-based early EG onset definition, EG eye orbital optic nerve axon loss ranged from +2 to −29% compared to the contralateral control eye. Thus, the level of damage present in all 4 study animals is likely below the 40% to 50% RGC somal loss required for manifest visual field loss in NHP EG.[66]

EG Eye ONH Myelin Protein Intensity was Decreased Within the Immediate Retrolaminar Orbital Optic Nerve in Early to Moderate NHP EG

Experiment-wide qIHC data for MBP and CNPase are reported for the RL1 and RL2 regions in Table 2 and Figure 5. Animal-specific statistical significance is also reported in Table 2. Animal-specific mean ± SD qIHC data are reported in Supplementary Table S1. Representative IHC images for

TABLE 2. Animal-Specific and Experiment-Wide ($n = 4$ NHPs) EG versus C Eye Expression Differences Within the Laminar and Retrolaminar Nerve (RL1, 0–250 µm and RL2, 251–500 µm)

NHP #	Region	MBP Intensity per unit area	CNPase Intensity per unit area	GFAP Intensity per unit area	Nuc Blue Pixel-cluster density	Iba1 (+) Pixel-cluster density
	Lamina	NP	NP	0.001	0.02	0.52
1	RL1	0.005	0.02	0.08	0.006	0.06
	RL2	0.15	NA	NA	NA	NA
	Lamina	NP	NP	0.12	0.63	0.86
2	RL1	<0.001	0.0001	0.02	0.02	0.06
	RL2	0.0007	0.0002	0.0011	0.01	0.009
	Lamina	NP	NP	0.03	0.18	0.002
3	RL1	0.03	0.02	0.21	0.55	0.55
	RL2	0.12	0.008	0.11	0.16	0.22
	Lamina	NP	NP	0.005	0.34	0.49
4	RL1	0.02	0.08	0.09*	0.001*	0.88*
	RL2	0.03	NA	NA	NA	NA
	Lamina	NP	NP	<0.001	0.008	0.03
Experiment wide (4 NHPs)	RL1	<0.001	<0.001	0.0011	0.0002	0.01
	RL2	<0.001	0.0004	0.0004	<0.001	0.002

P values are determined by mixed effects model. Decrease is represented as purple-filled boxes and increase is yellow-filled boxes. The *P* values that are close to *P* = 0.05 show the direction of change and are outlined in purple (decrease) or yellow (increase). Pixel cluster density were analyzed using Poisson distribution. Some animals had short retrolaminar neve in the paraffin sections therefore RL2 could not be analyzed and denoted by NA. NP = not present. * 3 posterior belts analyzed. Representative images from NHP2 are shown in Figures 6–10.

EG and control eye sections from NHP 2 are shown for MBP in Figure 6 and for CNPase in Figure 7. Experiment-wide control and EG eye heat maps and EG versus control eye percent difference maps are reported for both proteins in Figure 11.

MBP and CNPase signal intensity was assessed within independent qIHC runs in which the FoBMO sectoral location and orientation of the constituent sections were different (see Fig. 3, which documents this difference for NHP 2). Experiment-wide, MBP was decreased in EG eyes compared to control eyes by 31.4% in RL1 ($P < 0.001$) and 19.6% in RL2 ($P < 0.001$; see Table 2, Fig. 5). Animal-specific EG versus control eye decreases in MBP were significant in the RL1 region in all 4 NHPs, and the RL2 region of 2 out of 4 NHPs (see Table 2, Supplementary Table S1). Experiment-wide CNPase intensity was decreased in the EG eyes in RL1 62.3% ($P < 0.001$) and decreased in RL2 by 56.1% ($P = 0.0004$; see Table 2, and Fig. 5). CNPase intensity was significantly decreased in the EG eyes of 3 out of 4 NHPs in the RL1 region and in 2 NHPs in the RL2 region in which the optic nerve sample in the studied IHC sections was long enough to allow RL2 region analysis (see Table 2, Supplementary Table S1).

GFAP Intensity was Decreased and NucBlue and Iba1 Positive Pixel-Cluster Densities Were Increased Within the Laminar and Immediate Retrolaminar Orbital Optic Nerve

GFAP, NucBlue, and Iba1 were assessed within the same IHC sections (i.e. within the same qIHC run; see Fig. 3) and these individual findings are thus co-localized. Representative IHC images for EG and control eye sections from animal 2 are shown for GFAP in Figure 8, NucBlue in Figure 9, and Iba1 in Figure 10. Experiment-wide control and EG eye heat maps and EG versus control eye percent difference maps are reported in Figure 11.

Experiment-wide GFAP intensity was decreased in the lamina of EG eyes by 41.6% ($P < 0.001$), decreased in RL1 by 26.7% ($P = 0.001$), and decreased in RL2 by 28.4% ($P = 0.0004$; see Table 2, Supplementary Table S1). Animal-specific GFAP intensity was significantly decreased in EG eyes in the lamina in 3 out of the 4 NHPs, significantly decreased in the RL1 subregion in NHP 2, and significantly decreased in the RL2 region in 1 of the 2 NHPs that had RL2 tissue regions in the IHC sections (see Table 2, Supplementary Table S1).

Experiment-wide NucBlue pixel-cluster density was increased in the lamina of EG eyes by 16.6% ($P = 0.008$), increased in RL1 by 23.7% ($P = 0.0002$), and increased in RL2 by 33.2% ($P < 0.001$; see Table 2, Supplementary Table S1). Animal-specific NucBlue pixel-cluster density significantly increased in EG eyes within the lamina in 1 out of the 4 NHPs, significantly increased in the RL1 region in 3 out of the 4 NHPs, and significantly increased in the RL2 region of 1 out of the 2 NHPs that had RL2 tissue regions in the IHC sections (see Table 2, Supplementary Table S1).

Experiment-wide Iba1+ pixel-cluster density increased in the lamina of EG eyes by 28.2% ($P = 0.03$), increased in RL1 by 37.3% ($P = 0.01$), and increased in RL2 by 53.7% ($P = 0.002$; see Table 2, Supplementary Table S1). Animal-specific Iba1+ pixel-cluster density significantly increased in EG eyes within the lamina of 1 out of the 4 NHPs, increased in the RL1 region (with borderline significance) in 2 of the 4 NHPs, and significantly increased in the RL2 region of 1 of the 2 NHPs that had RL2 tissue regions in the IHC sections (see Table 2, Supplementary Table S1).

DISCUSSION

Retrolaminar Myelin-Related Protein Intensity Is Decreased in NHP Early to Moderate EG

We used qIHC to separately localize the alterations in CNPase and MBP within the immediate retrolaminar optic nerve tissues in early to moderate NHP EG. Because the animals in this study were euthanized at levels of OCT-detected RNFL thinning (see Table 1) that would not likely be associated with detectable visual field changes,[67,68] our data suggest that ONH myelin alterations may occur in the setting of early RGC axon damage and/or involve axons that are demyelinated but are still structurally and functionally intact. Scanning block face electron microscopic studies are underway to determine the structural status of the axons that are demyelinated in early EG (manuscript in preparation). Additional studies to determine the structural and functional status of demyelinated axons are required to assess if myelin-related protein alterations occur primarily and contribute to the pathophysiology of glaucomatous RGC axon damage or occur secondary to that damage. Regardless of whether their role in axonal insult is primary or secondary, if ONH myelin homeostasis is similarly disrupted in early human glaucoma, the goal of stabilizing ONH myelin homeostasis may provide neuroprotective or myeloprotective targets[69–71] for axonal preservation in ocular hypertension and early glaucoma that complement the effects of lowering IOP.

Disruption of Myelin Homeostasis in NHP Early EG May Be Accompanied by Decreases in GFAP Signaling and Increases in the Number of Nuclei and Iba1 Pixel-Cluster Densities

Because the CNPase and MBP qIHC runs were not performed in the same tissue sections as the GFAP, NucBlue, and Iba1 qIHC, we cannot say that the myelin (MBP/CNPase) and cellular (GFAP/NucBlue/Iba1) phenomena are "anatomically associated." The clinical location of the vertical MBP tissue sections (IHC run 1) was most commonly "central" within the neural canal for all animals and physically separate from the more peripheral and temporal neural canal location of the CNPase (IHC run 2) and GFAP/NucBlue/Iba1 (IHC run 3) tissue sections (see Fig. 3 and the Methods section). However, because the GFAP, NucBlue, and Iba1 qIHC were assessed within the same tissues sections these findings are anatomically associated with one another within the tissue regions we studied. Whereas the CNPase IHC (run 2) was done separately from the GFAP/NucBlue/Iba1 IHC (run 3), the CNPase tissue sections were either physically adjacent to the GFAP/NucBlue/Iba1 sections or physically close to them (i.e. within the same clinical region) in most instances. Follow-up studies in qIHC dedicated tissue sections from two new groups of early EG NHPs ($n = 4$ young and $n = 4$ old) will allow us to perform new qIHC runs in which these probes are assessed either in the same or immediately adjacent tissue sections in experiments designed to confirm colocalization of these phenomena.

Astrocyte "activation," supported by increased GFAP signal, hypertrophy, and proliferation have been described in multiple rodent[41,46,72–74] and NHP[21,75] reports. Extensive

axon loss correlates with gliosis and presence of reactive astrocytes in chronic mouse glaucoma.[46] Sun et al.[72] demonstrated that the astrocyte reactivity plays a protective function in preserving visual function in mice. Most of these reports likely describe a later stage of damage than the present study. However, Johnson et al.[76] reported decreased GFAP IHC signal at 7 and 14 days post IOP elevation in the rat unilateral EG model, and in a follow-up mRNA quantitation study of 5 stages of optic nerve axon loss,[8] reported no changes in GFAP expression at any of the 5 stages of damage. Johnson's initial report of early decreased GFAP[76] expression following acute IOP elevation, while was not present at any stage of orbital optic nerve axon loss in the later mRNA study,[8] is compatible with our findings and our working hypothesis that there is early astrocyte process withdrawal in NHP EG.

Cho et al.[77] used a rat model of acute high IOP and saw GFAP increases at the ONH 2 days post injury. Chrysostomou et al.[78] used a mouse manometric acute model for elevated IOP and saw GFAP increases at 1 and 7 days post insult. It is worth noting that acute changes in astrocytes may not predict the effects of chronic IOP elevation as profound morphologic alterations to astrocytes following acute IOP elevation reported by Sun et al. resolved after 7 days.[42] Localized changes in GFAP may differ peripherally compared to centrally within the neural canal and we may have detected a GFAP decrease because our tissue sections only sampled the peripheral portion of the neural canal. Future studies will more rigorously sample the inferior, central, and superior neural canal to further explore such regional differences.

Our study was not designed to assess the activation status of the astrocytes within our target ONH regions. Nor did we include studies of astrocyte nuclear markers, such as Sox2 and Pax2[79] to identify increases or decreases in astrocyte cell density. Because GFAP is an important cytoskeletal protein that is densely present in the astrocyte processes[73,80] we hypothesize that this finding represents either a withdrawal of astrocyte processes from the axon bundles or a primary alteration in the astrocyte process cytoskeleton. In both mouse[81] and rat[43,44] models of glaucoma, astrocyte processes have been reported to reorganize. In the DBA/2J genetic model of glaucoma, astrocyte processes are thickened, simplified, and have reduced spatial coverage.[41,81] Because, the astrocyte (and oligodendrocyte) processes are thought to play central roles in RGC axon nutrient delivery and myelin homeostasis[82] astrocyte process retraction may represent an abandonment of these homeostatic roles that may leave the RGC axon more vulnerable to compromised axon transport and injury.[42,83]

NucBlue and Iba1 Positive Pixel-Cluster Density Increases are Compatible With Previous Reports of Microglial Activation, Microgliosis,[84–86] and Myeloid Cell Invasion[27] in EG

Regarding the increase in NucBlue nuclear and Iba1+ pixel-cluster densities, whether triggered by demyelination, the mechanisms underlying demyelination, or other processes, there is strong evidence in the mouse and rat eye that activated microglia and blood borne central nervous system (CNS) myeloid cell infiltration within the ONH tissues is an early response to chronic IOP elevation.[87,88] Whereas this response may initially be protective, a series of reports have demonstrated that by blocking this response, RGC axons are

preserved.[89,90] Studies to identify links among phagocytosis of debris,[23] myeloid cell invasion,[26,27] and neuroinflammation[91,92] are underway.

Our findings should be interpreted in the context of the following limitations. First, our contralateral control eyes may themselves be altered due to the damage induced by chronic IOP elevation in the EG eye. Cooper et al.[4] have reported profound changes in the retrolaminar optic nerves of contralateral eyes in the mouse microbead unilateral experimental glaucoma model. Although this may be present in the NHP EG model, we have never seen longitudinal OCT detected RNFLT thinning in the control eyes of NHPs, including in those NHPs carried to moderate and severe stages of damage. Tribble et al.[93] have reported the presence of reactive microglia throughout the visual pathways in a rat model of unilateral experimental glaucoma. Dedicated studies to characterize control eye qIHC changes in the unilateral NHP EG model requiring comparison to age-matched, naive-normal eyes (i.e. from bilaterally normal animals) are necessary. However, it should be noted that any alterations induced in the contralateral control eyes would act to reduce the observed inter-eye differences, and so this caveat is unlikely to influence the conclusions of our study.

Second, our studies of the retrolaminar optic nerve were limited to only the RL1 and RL2 optic nerve tissue regions and follow-up studies will more consistently assess the complete 3 mm retrolaminar optic nerve stump (see Figs. 2, 3) for these same changes. Third, in one of the four NHPs of this study (NHP 3), it was retrospectively noted (after IHC had been completed), that the position of the EG eye sections for the GFAP, Iba1, and NucBlue where inadvertently selected from the mid-nasal rather than the mid-temporal ONH. Although the proper superior versus inferior orientation of these sections was confirmed, the EG versus control eye section locations were least well matched for these targets in NHP 3, which may have contributed to our inability to detect EG versus control eye differences in any of these targets within the retrolaminar regions of NHP 3 (see Fig. 4, Table 2). Fourth, whereas we believe the Iba1+ pixel clusters identified in this study represent Iba1+ cells, due to the thin (5 µm) sections, colocalization of the Iba1+ pixel clusters to NucBlue identified pixel clusters could not be performed. Because our thresholding method of identifying Iba1+ clusters was objective and identically applied to both the EG and control eyes, we believe that the EG eye increases in Iba1+ cluster density we report are biologically meaningful. However, follow-up studies that are designed to colocalize Iba1+ pixel-clusters to markers of cell nuclei are required. Finally, our characterization of astrocyte alteration in this study was limited to alterations in GFAP signaling only. A more complete characterization of astrocyte reactive status within ONH regions demonstrating varying levels of RNFLT and orbital optic nerve axon loss is planned using multiple colocalized markers, as has been recently discussed.[94]

In summary, we used qIHC to detect decreased intensity of CNPase and MBP within the retrolaminar tissues as well decreased astrocytic cytoskeletal protein GFAP within the laminar and retrolaminar ONH regions of NHP early to moderate EG eyes. We also found increases in Iba1 positive and NucBlue pixel-cluster densities within the laminar and retrolaminar regions of the same EG versus control eyes. Although our data does not allow us to co-localize these two sets of findings, EM and qIHC studies to determine if structurally intact RGC axons are demyelinated within the retro-

laminar optic nerve of NHP early EG eyes, to determine the cells and mechanisms responsible for demyelination, and to link these findings to co-localized longitudinal OCT ONH and RNFLT change are underway in our laboratory.

Acknowledgments

Disclosure: **P. Chaudhary**, None; **C. Stowell**, None; **J. Reynaud**, None; **S.K. Gardiner**, None; **H. Yang**, None; **G. Williams**, None; **I. Williams**, None; **N. Marsh-Armstrong**, None; **C.F. Burgoyne**, Heidelberg Engineering (F), Reichert (F)

References

1. Yucel YH, Gupta N. A framework to explore the visual brain in glaucoma with lessons from models and man. *Exp Eye Res*. 2015;141:171–178.
2. Davis BM, Crawley L, Pahlitzsch M, Javaid F, Cordeiro MF. Glaucoma: the retina and beyond. *Acta Neuropathol*. 2016;132(6):807–826.
3. Zhang HJ, Mi XS, So KF. Normal tension glaucoma: from the brain to the eye or the inverse? *Neural Regen Res*. 2019;14(11):1845–1850.
4. Cooper ML, Pasini S, Lambert WS, et al. Redistribution of metabolic resources through astrocyte networks mitigates neurodegenerative stress. *Proc Natl Acad Sci USA*. 2020;117(31):18810–18821.
5. Quigley HA, Addicks EM, Green WR, Maumenee AE. Optic nerve damage in human glaucoma. II. The site of injury and susceptibility to damage. *Arch Ophthalmol*. 1981;99(4):635–649.
6. Jakobs TC, Libby RT, Ben Y, John SW, Masland RH. Retinal ganglion cell degeneration is topological but not cell type specific in DBA/2J mice. *J Cell Biol*. 2005;171(2):313–325.
7. Howell GR, Libby RT, Jakobs TC, et al. Axons of retinal ganglion cells are insulted in the optic nerve early in DBA/2J glaucoma. *J Cell Biol*. 2007;179(7):1523–1537.
8. Johnson EC, Jia L, Cepurna WO, Doser TA, Morrison JC. Global changes in optic nerve head gene expression after exposure to elevated intraocular pressure in a rat glaucoma model. *Invest Ophthalmol Vis Sci*. 2007;48(7):3161–3177.
9. Minckler DS, Tso MO, Zimmerman LE. A light microscopic, autoradiographic study of axoplasmic transport in the optic nerve head during ocular hypotony, increased intraocular pressure, and papilledema. *Am J Ophthalmol*. 1976;82(5):741–757.
10. Minckler DS, Bunt AH, Johanson GW. Orthograde and retrograde axoplasmic transport during acute ocular hypertension in the monkey. *Invest Ophthalmol Vis Sci*. 1977;16(5):426–441. PMID: 67096.
11. Minckler DS, Spaeth GL. Optic nerve damage in glaucoma. *Surv Ophthalmol*. 1981;26(3):128–148. PMID: 6175030.
12. Quigley HA, Pitha IF, Welsbie DS, et al. Losartan Treatment Protects Retinal Ganglion Cells and Alters Scleral Remodeling in Experimental Glaucoma. *PLoS One*. 2015;10(10):e0141137.
13. Levin LA, Crowe ME, Quigley HA. Lasker/IRRF Initiative on Astrocytes and Glaucomatous Neurodegeneration Participants. Neuroprotection for glaucoma: Requirements for clinical translation. *Exp Eye Res*. 2017;157:34–37.
14. Nucci C, Martucci A, Giannini C, Morrone LA, Bagetta G, Mancino R. Neuroprotective agents in the management of glaucoma. *Eye (Lond)*. 2018;32(5):938–945.
15. Fernández-Albarral JA, Ramírez AI, de Hoz R, et al. Neuroprotective and Anti-Inflammatory Effects of a Hydrophilic Saffron Extract in a Model of Glaucoma. *Int J Mol Sci*. 2019;20(17):4110.
16. Adams CM, Stacy R, Rangaswamy N, Bigelow C, Grosskreutz CL, Prasanna G. Glaucoma - Next Generation Therapeutics: Impossible to Possible. *Pharm Res*. 2018;36(2):25.
17. Quaranta L, Riva I, Biagioli E, et al. CoQun Study Group. Evaluating the Effects of an Ophthalmic Solution of Coenzyme Q10 and Vitamin E in Open-Angle Glaucoma Patients: A Study Protocol. *Adv Ther*. 2019;36(9):2506–2514.
18. Burgoyne CF, Downs JC, Bellezza AJ, Suh JK, Hart RT. The optic nerve head as a biomechanical structure: a new paradigm for understanding the role of IOP-related stress and strain in the pathophysiology of glaucomatous optic nerve head damage. *Prog Retin Eye Res*. 2005;24(1):39–73.
19. Burgoyne CF. A biomechanical paradigm for axonal insult within the optic nerve head in aging and glaucoma. *Exp Eye Res*. 2011;93(2):120–132.
20. Yang H, Reynaud J, Lockwood H, et al. The connective tissue phenotype of glaucomatous cupping in the monkey eye - Clinical and research implications. *Prog Retin Eye Res*. 2017;59:1–52.
21. Hernandez MR. The optic nerve head in glaucoma: role of astrocytes in tissue remodeling. *Prog Retin Eye Res*. 2000;19(3):297–321.
22. Morgan JE. Optic nerve head structure in glaucoma: astrocytes as mediators of axonal damage. *Eye (Lond)*. 2000;14(Pt 3B):437–444.
23. Nguyen JV, Soto I, Kim KY, et al. Myelination transition zone astrocytes are constitutively phagocytic and have synuclein dependent reactivity in glaucoma. *Proc Natl Acad Sci USA*. 2011;108(3):1176–1181.
24. Yuan L, Neufeld AH. Activated microglia in the human glaucomatous optic nerve head. *J Neurosci Res*. 2001;64(5):523–532.
25. Tribble JR, Harder JM, Williams PA, John SWM. Ocular hypertension suppresses homeostatic gene expression in optic nerve head microglia of DBA/2J mice. *Mol Brain*. 2020;13(1):81.
26. Huang Y, Li Z, van Rooijen N, Wang N, Pang CP, Cui Q. Different responses of macrophages in retinal ganglion cell survival after acute ocular hypertension in rats with different autoimmune backgrounds. *Exp Eye Res*. 2007;85(5):659–666.
27. Margeta MA, Lad EM, Proia AD. CD163+ macrophages infiltrate axon bundles of postmortem optic nerves with glaucoma. *Graefes Arch Clin Exp Ophthalmol*. 2018;256(12):2449–2456.
28. Howell GR, Macalinao DG, Sousa GL, et al. Molecular clustering identifies complement and endothelin induction as early events in a mouse model of glaucoma. *J Clin Invest*. 2011;121(4):1429–1444.
29. Howell GR, Soto I, Zhu X, et al. Radiation treatment inhibits monocyte entry into the optic nerve head and prevents

neuronal damage in a mouse model of glaucoma. *J Clin Invest*. 2012;122(4):1246–1261.

30. Thale AB, Gordes RS, Rochels R, Tillmann B. Changes in extracellular matrix in the lamina cribosa of patients with secondary glaucoma. *Ophthalmologe*. 1996;93(5):586–591. Paper in German.

31. Liu B, McNally S, Kilpatrick JI, Jarvis SP, O'Brien CJ. Aging and ocular tissue stiffness in glaucoma. *Surv Ophthalmol*. 2018;63(1):56–74.

32. Son JL, Soto I, Oglesby E, et al. Glaucomatous optic nerve injury involves early astrocyte reactivity and late oligodendrocyte loss. *Glia*. 2010;58(7):780–789.

33. Roberts MD, Sigal IA, Liang Y, Burgoyne CF, Downs JC. Changes in the biomechanical response of the optic nerve head in early experimental glaucoma. *Invest Ophthalmol Vis Sci*. 2010;51(11):5675–5684.

34. Roberts MD, Grau V, Grimm J, et al. Remodeling of the connective tissue microarchitecture of the lamina cribrosa in early experimental glaucoma. *Invest Ophthalmol Vis Sci*. 2009;50(2):681–690.

35. Yang H, Williams G, Downs JC, et al. Posterior (outward) migration of the lamina cribrosa and early cupping in monkey experimental glaucoma. *Invest Ophthalmol Vis Sci*. 2011;52(10):7109–7121.

36. Mills EA, Davis CH, Bushong EA, et al. Astrocytes phagocytose focal dystrophies from shortening myelin segments in the optic nerve of Xenopus laevis at metamorphosis. *Proc Natl Acad Sci USA*. 2015;112(33):10509–10514.

37. Renner M, Stute G, Alzureiqi M, et al. Optic Nerve Degeneration after Retinal Ischemia/Reperfusion in a Rodent Model. *Front Cell Neurosci*. 2017;11:254.

38. Korneva A, Schaub J, Jefferys J, et al. A method to quantify regional axonal transport blockade at the optic nerve head after short term intraocular pressure elevation in mice. *Exp Eye Res*. 2020;196:108035.

39. Yücel YH, Kalichman MW, Mizisin AP, Powell HC, Weinreb RN. Histomorphometric analysis of optic nerve changes in experimental glaucoma. *J Glaucoma*. 1999;8(1):38–45.

40. Quillen S, Schaub J, Quigley H, Pease M, Korneva A, Kimball E. Astrocyte responses to experimental glaucoma in mouse optic nerve head. *PLoS One*. 2020;15(8):e0238104.

41. Wang R, Seifert P, Jakobs TC. Astrocytes in the Optic Nerve Head of Glaucomatous Mice Display a Characteristic Reactive Phenotype. *Invest Ophthalmol Vis Sci*. 2017;58(2):924–932.

42. Sun D, Qu J, Jakobs TC. Reversible reactivity by optic nerve astrocytes. *Glia*. 2013;61(8):1218–1235.

43. Tehrani S, Johnson EC, Cepurna WO, Morrison JC. Astrocyte processes label for filamentous actin and reorient early within the optic nerve head in a rat glaucoma model. *Invest Ophthalmol Vis Sci*. 2014;55(10):6945–6952.

44. Tehrani S, Davis L, Cepurna WO, et al. Astrocyte Structural and Molecular Response to Elevated Intraocular Pressure Occurs Rapidly and Precedes Axonal Tubulin Rearrangement within the Optic Nerve Head in a Rat Model. *PLoS One*. 2016;11(11):e0167364.

45. Ramirez AI, de Hoz R, Salobrar-Garcia E, Salazar JJ, et al. The Role of Microglia in Retinal Neurodegeneration: Alzheimer's Disease, Parkinson, and Glaucoma. *Front Aging Neurosci*. 2017;9:214.

46. Bosco A, Breen KT, Anderson SR, Steele MR, Calkins DJ, Vetter ML. Glial coverage in the optic nerve expands in proportion to optic axon loss in chronic mouse glaucoma. *Exp Eye Res*. 2016;150:34–43.

47. Burgoyne CF. The non-human primate experimental glaucoma model. *Exp Eye Res*. 2015;141:57–73.

48. He L, Yang H, Gardiner SK, et al. Longitudinal detection of optic nerve head changes by spectral domain optical coherence tomography in early experimental glaucoma. *Invest Ophthalmol Vis Sci*. 2014;55(1):574–586.

49. Pohlman RM, Turney MR, Wu PH, Brace CL, Ziemlewicz TJ, Varghese T. Two-dimensional ultrasound-computed tomography image registration for monitoring percutaneous hepatic intervention. *Med Phys*. 2019;46(6):2600–2609.

50. Anderson DR. Ultrastructure of human and monkey lamina cribrosa and optic nerve head. *Arch Ophthalmol*. 1969;82(6):800–814.

51. Anderson DR, Hoyt WF. Ultrastructure of intraorbital portion of human and monkey optic nerve. *Arch Ophthalmol*. 1969;82(4):506–530.

52. Hong S, Yang H, Gardiner SK, et al. OCT-Detected Optic Nerve Head Neural Canal Direction, Obliqueness, and Minimum Cross-Sectional Area in Healthy Eyes. *Am J Ophthalmol*. 2019;208:185–205.

53. Downs JC, Yang H, Girkin C, et al. Three-dimensional histomorphometry of the normal and early glaucomatous monkey optic nerve head: neural canal and subarachnoid space architecture. *Invest Ophthalmol Vis Sci*. 2007;48(7):3195–3208.

54. Strouthidis NG, Yang H, Fortune B, Downs JC, Burgoyne CF. Detection of optic nerve head neural canal opening within histomorphometric and spectral domain optical coherence tomography data sets. *Invest Ophthalmol Vis Sci*. 2009;50(1):214–223.

55. Fortune B, Reynaud J, Hardin C, Wang L, Sigal IA, Burgoyne CF. Experimental Glaucoma Causes Optic Nerve Head Neural Rim Tissue Compression: A Potentially Important Mechanism of Axon Injury. *Invest Ophthalmol Vis Sci*. 2016;57(10):4403–4411.

56. He L, Ren R, Yang H, et al. Anatomic vs. acquired image frame discordance in spectral domain optical coherence tomography minimum rim measurements. *PLoS One*. 2014;9(3):e92225.

57. Yang H, Downs JC, Girkin C, et al. 3-D histomorphometry of the normal and early glaucomatous monkey optic nerve head: lamina cribrosa and peripapillary scleral position and thickness. *Invest Ophthalmol Vis Sci*. 2007;48(10):4597–4607.

58. Yang H, Downs JC, Bellezza A, Thompson H, Burgoyne CF. 3-D histomorphometry of the normal and early glaucomatous monkey optic nerve head: prelaminar neural tissues and cupping. *Invest Ophthalmol Vis Sci*. 2007;48(11):5068–5084.

59. Yang H, Downs JC, Sigal IA, Roberts MD, Thompson H, Burgoyne CF. Deformation of the normal monkey optic nerve head connective tissue after acute IOP elevation within 3-D histomorphometric reconstructions. *Invest Ophthalmol Vis Sci*. 2009;50(12):5785–5799.

60. Yang H, Reynaud J, Lockwood H, et al. 3D Histomorphometric Reconstruction and Quantification of the Optic Nerve Head Connective Tissues. *Methods Mol Biol*. 2018;1695:207–267.

61. Vincent L., Soille P. Watersheds in digital spaces: an efficient algorithm based on immersion simulations. *IEEE Transactions on Pattern Analysis and Machine Intelligence*, 1991;13(6), 583–598.

62. Schneider CA, Rasband WS, Eliceiri KW. NIH Image to ImageJ: 25 years of image analysis. *Nat Methods*. 2012;9(7):671–675.

63. Pinheiro J, Bates D. *Mixed-effects models in S and S-PLUS*. New York, NY: Springer Science & Business Media; 2006.

64. Fortune B, Cull G, Reynaud J, Wang L, Burgoyne CF. Relating Retinal Ganglion Cell Function and Retinal Nerve Fiber Layer (RNFL) Retardance to Progressive Loss of RNFL Thickness and Optic Nerve Axons in Experimental Glaucoma. *Invest Ophthalmol Vis Sci*. 2015;56(6):3936–3944.

65. Fortune B, Hardin C, Reynaud J, et al. Comparing Optic Nerve Head Rim Width, Rim Area, and Peripapillary Retinal Nerve Fiber Layer Thickness to Axon Count in Experimental Glaucoma. *Invest Ophthalmol Vis Sci*. 2016;57(9):OCT404–OCT412.

66. Harwerth RS, Crawford ML, Frishman LJ, Viswanathan S, Smith EL, 3rd, Carter-Dawson L. Visual field defects and neural losses from experimental glaucoma. *Prog Retin Eye Res*. 2002;21(1):91–125.

67. Harwerth RS, Vilupuru AS, Rangaswamy NV, Smith EL, 3rd. The relationship between nerve fiber layer and perimetry measurements. *Invest Ophthalmol Vis Sci*. 2007;48(2):763–773.

68. Cull GA, Reynaud J, Wang L, Cioffi GA, Burgoyne CF, Fortune B. Relationship between orbital optic nerve axon counts and retinal nerve fiber layer thickness measured by spectral domain optical coherence tomography. *Invest Ophthalmol Vis Sci*. 2012;53(12):7766–7773. Erratum in: Invest Ophthalmol Vis Sci. 2014 Apr;55(4):2619-20.

69. Chaudhary P, Marracci GH, Calkins E, et al. Thyroid hormone and thyromimetics inhibit myelin and axonal degeneration and oligodendrocyte loss in EAE. *J Neuroimmunol*. 2021;352:577468.

70. Hartley MD, Banerji T, Tagge IJ, et al. Myelin repair stimulated by CNS-selective thyroid hormone action. *JCI Insight*. 2019;4(8):e126329.

71. Chaudhary P, Marracci G, Yu X, Galipeau D, Morris B, Bourdette D. Lipoic acid decreases inflammation and confers neuroprotection in experimental autoimmune optic neuritis. *J Neuroimmunol*. 2011;233(1-2):90–96.

72. Sun D, Moore S, Jakobs TC. Optic nerve astrocyte reactivity protects function in experimental glaucoma and other nerve injuries. *J Exp Med*. 2017;214(5):1411–1430.

73. Sun D, Jakobs TC. Structural remodeling of astrocytes in the injured CNS. *Neuroscientist*. 2012;18(6):567–588.

74. Cooper ML, Crish SD, Inman DM, Horner PJ, Calkins DJ. Early astrocyte redistribution in the optic nerve precedes axonopathy in the DBA/2J mouse model of glaucoma. *Exp Eye Res*. 2016;150:22–33.

75. Hashimoto K, Parker A, Malone P, Gabelt BT, Rasmussen C, Kaufman PS, Hernandez MR. Long-term activation of c-Fos and c-Jun in optic nerve head astrocytes in experimental ocular hypertension in monkeys and after exposure to elevated pressure in vitro. *Brain Res*. 2005;1054(2):103–115.

76. Johnson EC, Deppmeier LM, Wentzien SK, Hsu I, Morrison JC. Chronology of optic nerve head and retinal responses to elevated intraocular pressure. *Invest Ophthalmol Vis Sci*. 2000;41(2):431–442.

77. Cho KJ, Kim JH, Park HY, Park CK. Glial cell response and iNOS expression in the optic nerve head and retina of the rat following acute high IOP ischemia-reperfusion. *Brain Res*. 2011;1403:67–77.

78. Chrysostomou V, Crowston JG. The photopic negative response of the mouse electroretinogram: reduction by acute elevation of intraocular pressure. *Invest Ophthalmol Vis Sci*. 2013;54(7):4691–4697.

79. Lozano DC, Choe TE, Cepurna WO, Morrison JC, Johnson EC. Early Optic Nerve Head Glial Proliferation and Jak-Stat Pathway Activation in Chronic Experimental Glaucoma. *Invest Ophthalmol Vis Sci*. 2019;60(4):921–932.

80. Sun D, Lye-Barthel M, Masland RH, Jakobs TC. The morphology and spatial arrangement of astrocytes in the optic nerve head of the mouse. *J Comp Neurol*. 2009;516(1):1–19.

81. Lye-Barthel M, Sun D, Jakobs TC. Morphology of astrocytes in a glaucomatous optic nerve. *Invest Ophthalmol Vis Sci*. 2013;54(2):909–917.

82. Butt AM, Pugh M, Hubbard P, James G. Functions of optic nerve glia: axoglial signalling in physiology and pathology. *Eye (Lond)*. 2004;18(11):1110–1121.

83. Sun D, Lye-Barthel M, Masland RH, Jakobs TC. Structural remodeling of fibrous astrocytes after axonal injury. *J Neurosci*. 2010;30(42):14008–14019.

84. Ebneter A, Casson RJ, Wood JP, Chidlow G. Microglial activation in the visual pathway in experimental glaucoma: spatiotemporal characterization and correlation with axonal injury. *Invest Ophthalmol Vis Sci*. 2010;51(12):6448–6660.

85. Bosco A, Romero CO, Breen KT, et al. Neurodegeneration severity can be predicted from early microglia alterations monitored in vivo in a mouse model of chronic glaucoma. *Dis Model Mech*. 2015;8(5):443–455.

86. Bosco A, Steele MR, Vetter ML. Early microglia activation in a mouse model of chronic glaucoma. *J Comp Neurol*. 2011;519(4):599–620.

87. Ludwin SK. Phagocytosis in the rat optic nerve following Wallerian degeneration. *Acta Neuropathol*. 1990;80(3):266–273.

88. Huang Y, Li Z, van Rooijen N, Wang N, Pang CP, Cui Q. Different responses of macrophages in retinal ganglion cell survival after acute ocular hypertension in rats with different autoimmune backgrounds. *Exp Eye Res*. 2007;85(5):659–666.

89. Schwartz M. Modulating the immune system: a vaccine for glaucoma? *Can J Ophthalmol*. 2007;42(3):439–441.

90. Bell K, Und Hohenstein-Blaul NVT, Teister J, Grus F. Modulation of the Immune System for the Treatment of Glaucoma. *Curr Neuropharmacol*. 2018;16(7):942–958.

91. Soto I, Howell GR. The complex role of neuroinflammation in glaucoma. *Cold Spring Harb Perspect Med*. 2014;4(8):a017269.

92. Williams PA, Marsh-Armstrong N, Howell GR Lasker/IRRF Initiative on Astrocytes and Glaucomatous Neurodegeneration Participants. Neuroinflammation in glaucoma: A new opportunity. *Exp Eye Res*. 2017;157:20–27.

93. Tribble JR, Kokkali E, Otmani A, et al. When Is a Control Not a Control? Reactive Microglia Occur Throughout the Control Contralateral Pathway of Retinal Ganglion Cell Projections in Experimental Glaucoma. *Transl Vis Sci Technol*. 2021;10(1):22.

94. Escartin C, Galea E, Lakatos A, et al. Reactive astrocyte nomenclature, definitions, and future directions. *Nat Neurosci*. 2021;24(3):312–325.